

Physical conditions in diffuse interstellar medium of local and high redshift galaxies: measurements based on excitation of H₂ rotational and C I fine-structure levels.

V.V. Klimenko¹ and S.A. Balashev¹

¹*Ioffe Institute, Polytekhnicheskaya ul. 26, 194021 Saint Petersburg, Russia – email: s.balashev@gmail.com*

5 August 2020

ABSTRACT

We present results of analysis of physical conditions (number density, intensity of UV field, kinetic temperature) in the cold H₂-bearing interstellar medium of local and high redshift galaxies. Our measurements based on the fit to the observed population of H₂ rotational levels and C I fine-structure levels with the help of grids of numerical models calculated with the PDR Meudon code. A joint analysis of low H₂ rotational levels and C I fine-structure levels allows to break the degeneracy in the $I_{UV} - n_{\text{H}}$ plane and provides significantly tighter constraints on the number density and intensity of UV field. Using archive data from the VLT/UVES, KECK/HIRES, HST/STIS and FUSE telescopes we selected 12 high redshift damped Ly α systems (DLAs) in quasar spectra and 14 H₂ absorption systems along the lines of sight towards stars in the Milky-Way and the Magellanic Clouds galaxies. These systems have strong H₂ components with the column density $\log N(\text{H}_2)/\text{cm}^{-2} > 18$ and associated C I absorptions. We find that H₂-bearing medium in high redshift DLAs and in local galaxies has similar values of the kinetic temperatures $T_{\text{kin}} \sim 100$ K and number density $10 - 500 \text{ cm}^{-3}$. However, the intensity of incident UV radiation in DLAs is varied in the wide range (0.1 – 100 units of Mathis field), while it is $\sim 0.1 - 3$ units of Mathis field for H₂ systems in Milky-Way and LMC and SMC galaxies. The large dispersion of measured UV flux in DLAs is probably a consequence that DLA sample probes the galaxies selected from the overall galaxy population at high- z and therefore corresponds to the wide range of the physical conditions.

Key words: cosmology: observations – quasar: absorption lines – ISM: clouds, molecules

1 INTRODUCTION

The absorption line analysis towards background sources is a powerful method to study local physical conditions in the interstellar medium (ISM). It has some advantages over emission line studies, in particular, it provides column density measurements over very small transverse scales. In the local Universe this corresponds to the extra tiny radius of stars, but even for remote Universe the sizes of emitting region of quasars (< 1 pc) and gamma-ray burst afterglows are significantly smaller than typical spatial resolution of emission line studies. Additionally, high resolution spectra enable to resolve absorption lines and therefore determine column densities with very high accuracy (< 0.1 dex). Another important aspect, that absorption line studies allow us to directly probe H₂ (along with many other associated species) through resonant rest-frame UV lines, the so-called Lyman and Werner bands. This leads that this technique is a perfectly suitable to study diffuse phases of the cold ISM,

which are very hardly accessible through emission studies, even in our own galaxy. This include so-called "CO-dark" gas which can be the dominant form of the molecular gas at low metallicities (Balashev et al. 2017). Usually, the optical and especially UV wavelength range is suitable for the absorption line studies, since most of resonant permitted electronic transitions are located in these ranges. For the high redshift measurement it provides even more advantage, since UV range due to cosmological redshift is shifted in optical domain, which allows to obtain high resolution spectra at the largest ground-based optical telescopes (Noterdaeme et al. 2008).

To determine *local* physical conditions one can use the measurements of the relative population of the energy levels of the different species. For the cold diffuse ISM, with typical temperatures $\lesssim 100$ K, the most appropriate energy systems are rotational levels of H₂, HD (e.g. Balashev et al. 2010) and fine-structure levels of C I, C II, Si II and O I (see e.g.

Silva & Viegas 2002). However, O I has a relatively large distance between the fine-structure levels, and therefore lines from excited levels of O I is observed very seldom. Additionally, usually, it is very hard to constrain the column density even for the ground level of O I, since available resonant UV lines are usually saturated. While the fine-structure excitation of Si II is not very often observed in DLAs in contrast to C II, they were both analysed in several DLAs (Srianand & Petitjean 2000; Howk et al. 2005; Kulkarni et al. 2012; Neeleman et al. 2015). However for both Si II and C II even if available always correspond to the mix of the cold and warm phases (e.g. Neeleman et al. 2015). In contrast to O I and Si II, the excitation of C I fine-structure levels is a perfect tracer of the cold diffuse ISM. Historically, it was used to measure the thermal pressure in the cold ISM in the Milky Way (MW, Jenkins & Tripp 2011), Magellanic clouds (MC, Welty et al. 2016) and in low (Muzahid et al. 2016) and high redshift DLAs (Srianand et al. 2005; Jorgenson et al. 2010; Balashev et al. 2019).

The population of H₂ levels also is perfectly suitable for the determination of the physical condition of the cold diffuse ISM. Such measurements, usually requires the computational expensive modelling of the cold ISM including detailed radiative transfer in resonant H₂ lines, which are typically in optically thick regime. The latter results in that excitation of H₂ levels are highly homogeneous within the cloud (Abgrall et al. 1992; Balashev et al. 2009). However, for saturated H₂ absorption systems, with $\log N(\text{H}_2) > 18$ (where N is column density measured in cm^{-2}), the levels of $J=0,1,2$ are predominantly thermalized and their excitation is typically close to the thermal temperature (Le Petit et al. 2006), which is set by the thermal balance, itself being a function of the density and UV field. Indeed, the main heating mechanism in the diffuse neutral ISM is a photoelectric effect on grains, whereas cooling is a combination of the emission in C II and O I lines and electron recombination (Draine 2011). Rates of these processes are strongly dependent on the gas density, metallicity and intensity of UV radiation. On the other hand, the excitation of higher rotational levels of H₂ at $J \geq 3$ is determined mainly by the UV pumping (Black & Dalgarno 1976) and regulated by the intensity of UV radiation. Therefore, populations of both low and high rotational levels of H₂ carry information on the physical conditions, that makes them a promising tool for estimation physical parameters in the diffuse ISM.

However, with aforementioned difficulties, H₂ was previously used to estimate physical condition (number density and UV intensity) only in the specific cases in interstellar clouds in the Milky-Way (e.g. Jura 1975a,b; Nehmé et al. 2008) and in a few high-redshift H₂-bearing DLAs, whose analysis includes detailed and complex modeling of a single system (Noterdaeme et al. 2007; Klimenko et al. 2016; Rawlins et al. 2016; Noterdaeme et al. 2017; Rawlins et al. 2018; Shaw & Ferland 2020).

In this paper we present a systematic study of physical conditions in the cold ISM of high redshift and local galaxies based on the analysis of excitation of the rotational levels of H₂ and the fine-structure levels of C I. For these we used all available detected high redshift DLAs and sample of absorption systems in stellar spectra of the Milky-Way and Magellanic Clouds. The structure of the paper is following. In Sect. 2 we describe a method to analyse physical con-

ditions of molecular gas using observed populations of H₂ rotational levels and fine-structure levels of C I. The data of known H₂ and C I absorption systems in high redshift DLAs and local galaxies is compiled in Sect. 3. In Sect. 4 we present our measurements of the number density, kinetic temperature and intensity of the incident UV field in the samples. Then we discuss the dependencies of the inferred parameters and compare the measurements in local Universe and high redshift DLAs, before we conclude in Sect. 5.

2 METHOD

The excitation of most H₂ levels in the cold diffuse ISM is determined predominantly by the UV pumping that takes place in resonant UV lines. At typical H₂ column densities in observed absorption systems ($\log N(\text{H}_2) \gtrsim 16$), the UV lines can be significantly saturated, and hence, the excitation strongly varied within the cloud. Therefore the modelling of the excitation of H₂ levels requires an accurate calculation of radiative transfer to take into account shielding of H₂ absorption lines. Additionally, the population of the lower H₂ rotational levels ($J \leq 2$) can depend on the temperature of the gas, which also can be varied within the cloud, due to changes in the chemical state (e.g. HI/H₂ transition) and dilution of the UV field. Therefore we used the PDR MEUDON CODE¹ (Le Petit et al. 2006), which performs a complete calculation of the radiative transfer of UV radiation in the UV lines of H₂ in combination with a solution of the thermal balance and chemistry. A model consists of a slab cloud of the gas irradiated by isotropic interstellar radiation field from both sides. We adopted the standard model of the interstellar radiation (ISRF) proposed by Mathis et al. (1983). This ISRF covers a large wavelength range, from 912 Å to sub-millimeter. The intensity of the ISRF in the UV range was scaled by a factor I_{UV} . That is, $I_{\text{UV}} = 1$ corresponds to one unit of Mathis field or 0.75 unit of the Draine field (Draine 1978) in the interval between 912 Å-1100 Å. The cosmic microwave background (CMB) radiation is also the important component of the ISRF. The direct excitation by the CMB photons can be dominating mechanism of excitation of the first fine-structure level of C I in diffuse gas at high redshift (e.g. Silva & Viegas 2002). Therefore we used two set of PDR models calculated with different CMB temperatures $T_{\text{CMB}} = 2.73 \times (1+z)$ at $z=0$ for comparison with data samples of MW and MC measurements ($T_{\text{CMB}} = 2.73 \text{ K}$), and at average redshift $z = 2.5$ for comparison with a sample of high redshift systems ($T_{\text{CMB}} = 9.56 \text{ K}$). The full range of the redshift of high redshift DLAs sample is $2.0 < z_{\text{abs}} < 3.3$. The difference of the redshifts between absorption systems and the models introduces a systematic bias of the estimate of the number density (or thermal pressure). However this bias rapidly vanish with an increase of the number density, since collisional excitation starts to dominate in C I populations. We checked that for the studied systems this bias is not significantly larger than 0.2 dex, which is the typical statistical uncertainty of the present method.

The size of the modelled cloud was defined by the visual extinction $A_{\text{V}}^{\text{max}}$ parameter. We fixed it to $A_{\text{V}}^{\text{max}} = 0.5$ that

¹ We use a version 1.5.4 rev 2053 (from 03 March 2020)

corresponds to the total hydrogen column density $N(\text{H})_{\text{tot}} \approx 10^{21}/Z \text{ cm}^{-2}$, where Z is the metallicity. This maximal value exceeds the typical visual extinctions measured at high- z DLAs (e.g. Ledoux et al. 2015). For comparison with MW and MC measurements we used calculations with $A_V^{\text{max}} = 2.0$. Cosmic-ray ionization rate is assumed to be fixed and equal to 10^{-16} s^{-1} that has been estimated for diffuse clouds in Milky-Way (Indriolo et al. 2007). The input parameters for the PDR code are listed in Table 1. For each model we performed 25 iterations to obtain a stable solution of a cloud structure. Additionally, a convergence of the calculations for each model was checked visually.

An example of a PDR model with $Z = 0.1$, $n_{\text{H}} = 2 \times 10^2 \text{ cm}^{-3}$ and $I_{\text{UV}} = 0.7$ is shown in Fig. 1. One can see that population of H_2 rotational levels in this model are well agree with observed ones (shown in the bottom left panel of Fig. 1) in the absorption system at $z = 2.626443$ towards QSO J0812+3208 (Balashev et al. 2010, J0812+3208 A) at the size of the cloud corresponding to the total H_2 column density $\log N(\text{H}_2) = 19.9$, which is close to the measured one. At this depth the relative populations of C I fine-structure levels, are slightly higher than measured in the J0812+3208 A (shown in the bottom right panel of Fig. 1). One can also note that at the mild H_2 column densities, $\log N(\text{H}_2) \lesssim 19$ (typical for studied systems), excitation of C I fine-structure levels are more or less constant within the cloud. The drop in the population ratios of C I in the cloud interior is attributed with the temperature drop (see the left top panel of Fig. 1).

We ran grids of slab constant-density models in which we varied three parameters - the metallicity (Z , assuming dust scales to metallicity), total hydrogen number density (n_{H}) and intensity of UV radiation (I_{UV}). The kinetic temperature, chemical composition, and excitation of the levels were calculated self-consistently by PDR Meudon. To facilitate the representation of the results, for each metallicity in a set [-1.0, -0.5, 0.0, 0.5], we calculate grid of models that uniformly covers the parameter space on a logarithmic scale in the ranges of $0 \leq \log n_{\text{H}}/\text{cm}^{-3} \leq 4$ (with 10 points) and $-1 \leq \log I_{\text{UV}} \leq 3$ (with 9 points).

To compare observed populations of H_2 and C I levels in some absorption system with PDR models we firstly choose an appropriate $I_{\text{UV}} - n_{\text{H}}$ grid with metallicity closest to the observed one. Then within chosen grid we calculated the likelihood function based on least-square comparison of observed and model population of levels. To obtain the model population of H_2 and C I levels we determine a depth, where the total measured H_2 column density, calculated from one side of the model, equals to half the observed one. Then we calculated column densities of H_2 rotational levels at determined depth, and double the results. This approach mimics a cloud illuminated on both sides with ISRF scaled by I_{UV} factor and with the total column density of H_2 equal to the measured one. In order to obtain a smooth representation of the results in $n_{\text{H}} - I_{\text{UV}}$ plane, we use an interpolation of the populations in the calculated grid to the denser grid.

For comparison of H_2 rotational levels calculated by PDR code with the observed ones we added a factor of 2 (0.3 dex) systematic uncertainty to the observed column densities. This was done to relax the choice of an slab geometry in the modelling. Indeed the UV pumping of H_2 strongly depends on the saturation of Lyman and Werner lines, which

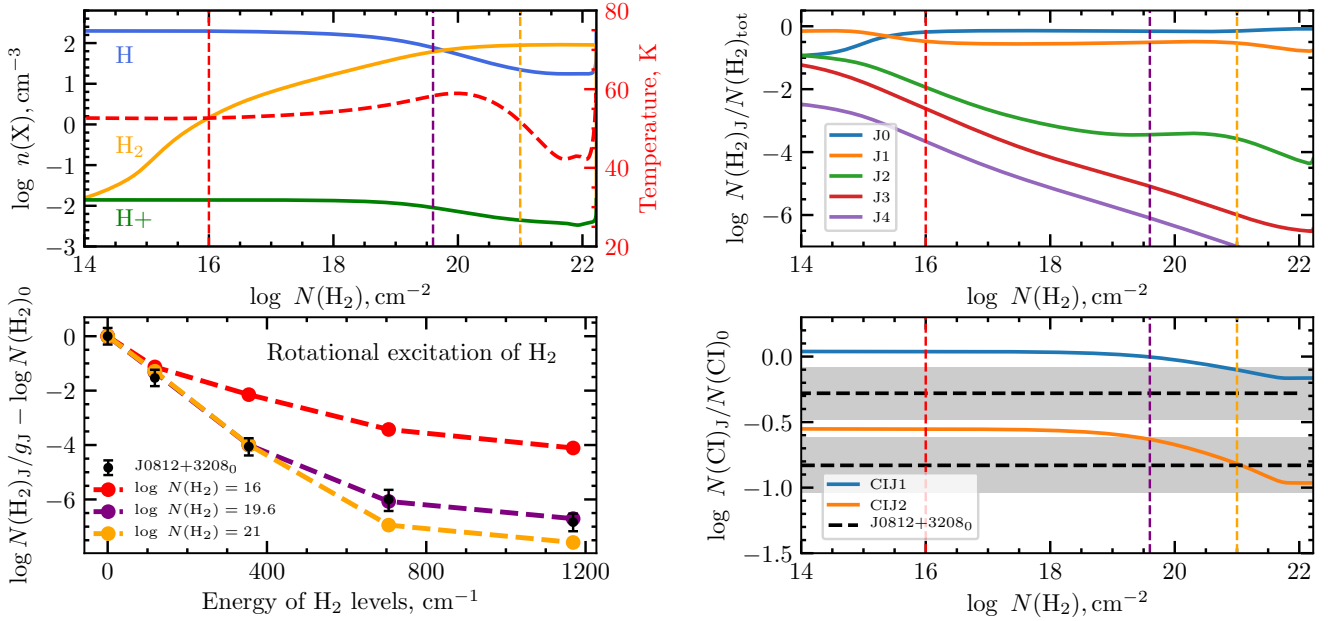
depends in turn on the H_2 column densities. Therefore the real geometry and its deviation from the simplistic shape typically used in modelling (e.g. slab or spherical) can induce a systematic uncertainty, which we tried to account for with this simplistic 0.3 dex factor. A similar systematic was found by Sternberg et al. (2014), where authors compared various types of geometry (slab, complex, sphere) and found that the difference of the molecular fraction along the line of sight is not higher than 40% for models with the same H I optical depth. This difference is accounted to various structure of H I- H_2 transition region, from which the major part of the observed high H_2 rotational levels are originated. Therefore, following Sternberg et al. (2014) we assumed that a factor of 2 is a good conservative choice to take into account the systematic uncertainty concerned with an unknown geometry of the cloud.

For C I we compared the relative population of fine structure levels. We use the relative populations, since the absolute abundance of C I is usually hard to reproduce in modelling, since it is determined by the ionization balance of carbon atoms in the ISM (e.g. Jenkins & Tripp 2011), and therefore it depends on many other parameters, such as the ionization fraction, dust properties and carbon abundance, which are usually poorly constrained in observations. However, for studied absorption systems the majority of the UV lines, at which excitation of C I fine-structure levels takes place are usually optically thin. Therefore the UV excitation of C I is little dependent on total abundance of C I (i.e. the location and C I/C II transition in the cloud) and hence it can be used to constrain UV flux. Therefore we argue that the relative populations of C I fine-structure levels is a good tracer of the physical conditions (UV flux, number density and temperature) inside the cloud.

An example of the constraints on the number density and UV intensity using excitation of H_2 rotational and C I fine-structure levels is shown in the top panels of Fig. 2 (for the J0812+3208 A). To show how the various combination of H_2 and C I levels constrain the parameter space we plot series of the panels. The best fits to the populations of selected H_2 and C I levels are shown in the bottom panels of Fig. 2. The lower rotational levels of H_2 $J=0, 1, 2$ (the left panel of Fig. 2) in saturated systems usually correspond to the kinetic temperature in the cloud, and therefore the obtained constraint in $I_{\text{UV}} - n_{\text{H}}$ plane reflects the excitation temperature T_{0-2} of H_2 . In the reasonable range of the number densities corresponded to the cold diffuse medium ($\log n_{\text{H}} \sim 2-3$) this translates in almost linear dependence between I_{UV} and n_{H} (see the left column of Fig. 2). Adding to $J=0,1,2$ H_2 levels the population of higher H_2 ($J=3$ and $J=4$) rotational levels, results in tighter constraints on the $I_{\text{UV}} - n_{\text{H}}$ region (see central panels in Fig. 2). This is mainly, since the UV pumping is the main mechanism of excitation of high rotational levels of H_2 (Black & Dalgarno 1976), therefore their populations are very sensitive to the intensity of UV radiation. The constraints on $I_{\text{UV}} - n_{\text{H}}$ using C I fine-structure is shown in the right panel in Fig. 2. In most cases C I gives quite wide degenerate region in $I_{\text{UV}} - n_{\text{H}}$ plane, but it typically is nearly orthogonal to the region constrained using H_2 (see also Balashev et al. 2019). Therefore a joint C I- H_2 fit allows us to break the degeneracy and provides significantly tighter constraints. Note that, in a case of J0812+3208 A a

Table 1. List of input parameters for the PDR Meudon models. The first three parameters (n_{H} , Z , I_{UV}) were varied within indicated ranges

Parameter	Units	Value	Comment
n_{H}	cm^{-3}	$1 - 10^4$	Total hydrogen number density
Z	solar	$0.1 - 3$	Metallicity
I_{UV}	Mathis field	$0.1 - 1000$	UV radiation strength
I_{CR}	s^{-1}	10^{-16}	Cosmic ray ionization rate
A_{Vmax}		0.5-2	Maximum visual extinction
v_{turb}	km s^{-1}	2	Gas turbulent velocity
T_{CMB}	K	2.73, 9.56	CMB temperature
Ext	Galaxy		Type of extinction curve
R_{V}		3.1	Ratio of the visual extinction to color excess
C_{D}	cm^{-2}	$5.8 \times 10^{21}/Z$	Ratio of the column density of neutral gas to visual extinction
m_{gr}		$0.01 \times Z$	Dust to gas mass ratio
q_{PAH}		4.6×10^{-2}	Polycyclic aromatic hydrocarbon fraction
α_{gr}		3.5	Grain power-law distribution index
r_{min}	cm	10^{-7}	Grains minimum radius
r_{max}	cm	3×10^{-5}	Grains maximum radius

**Figure 1.** An example of molecular cloud model with the Meudon PDR code. The top left panel presents the number densities of H, H₂ and H⁺ and the temperature (with red dashed line) as a function of the total H₂ column density. In the top and bottom right panels we show the profiles of the relative populations of H₂ rotational levels and C I fine structure levels, respectively. The bottom left panel shows the comparison of H₂ rotational level excitation calculated for three threshold depths, $\log N(\text{H}_2) = 16, 19.6$ and 21 , which are shown by vertical dashed lines in the right panels. The column densities are normalized using the statistical weight of H₂ rotational levels, $g(J)$. For comparison, the observed excitation of H₂ and C I levels in the absorption system at $z = 2.626443$ towards QSO J0812+3208 are shown by black circles and gray stripes in the bottom left and bottom right panels, respectively.

joint fit is well consistent with the constraint obtained with H₂ levels alone.

2.1 Note on excitation of high H₂ rotational levels.

In some absorption systems we were not able to describe simultaneously and self-consistently the excitation of rotational levels of H₂ and fine-structure levels of C I within

a one-component PDR model. For illustration, in Fig. 3 we show an example of such problematic fit for H₂-bearing DLA towards QSO J 1232+0815. We found that in this system the population of high rotational levels of H₂ (at $J=3, 4, 5$) is relatively enhanced. In one component model such an excitation gives the UV intensity about 10 times higher than Mathis field. To satisfy the thermal balance and kinetic temperature ($T_{01} \sim 70 \text{ K}$, which is mostly constrained by low rotational levels of H₂), a high gas density, $n_{\text{H}} \sim 10^3 \text{ cm}^{-3}$,

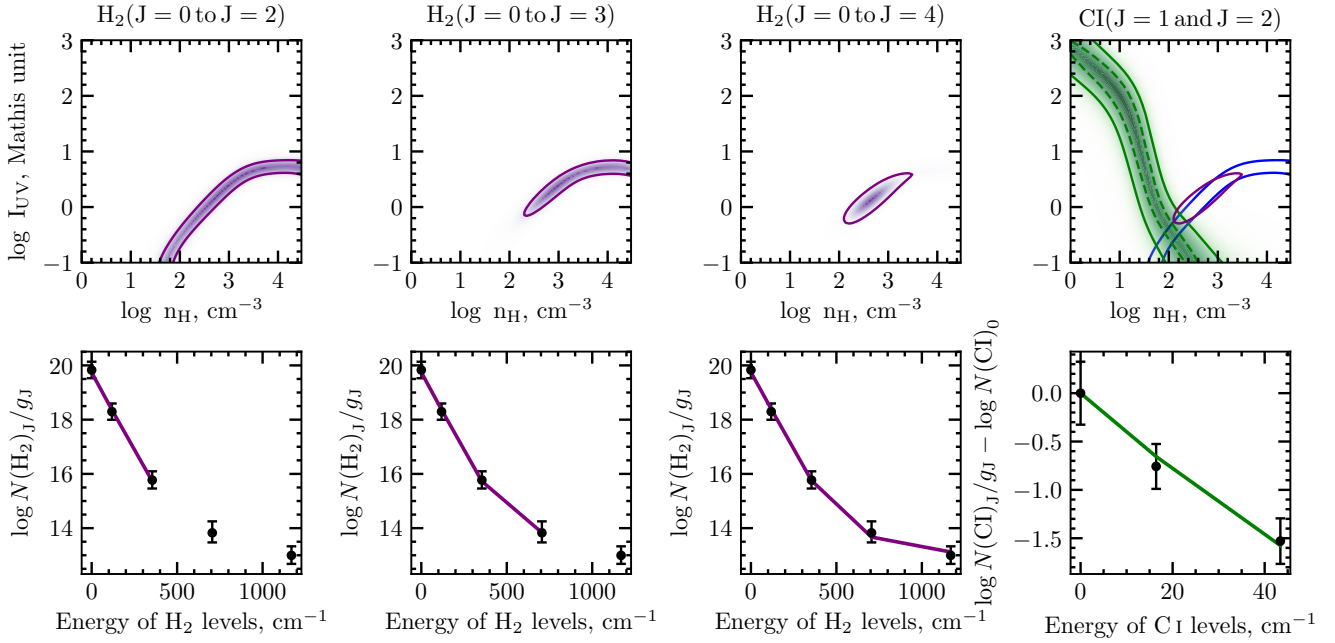


Figure 2. An example of the the analysis of excitation of H_2 rotational and $C I$ fine structure levels in the absorption system J0812+3208 A. The left and central panels correspond to fit to populations of various number of H_2 rotational levels, which is marked at the top. The right panels correspond to fit to the relative population of $C I$ fine structure levels. In top panels we show the constraints on the number density and UV intensity using excitation of marked levels. The probability density is represented by the colour intensity (purple for H_2 and green for $C I$), with the 68% confidence level contour shown as the solid line. For $C I$ we additionally show 30% confidence level by the green dashed line. For best comparison we overplot H_2 constraints obtained with fit to ($J=0$ to $J=2$) and ($J=0$ to $J=4$) levels with the blue and purple contours in the top right panel. In bottom panels we show respectively best fits to the populations of H_2 and $C I$ levels using purple and green lines. The observed population of H_2 levels and $C I$ levels are shown by black dots. Column densities normalized using the statistical weight g_J of H_2 and $C I$ levels. For $C I$ we normalized populations to the population of the ground $C I(J=0)$ level as well.

is required. At such physical conditions excited $C I$ levels should be significantly populated, much higher than it is really observed.

To reconcile this discrepancy more complex model should be invoked. This discrepancy is most likely arisen from the fact that different H_2 rotational levels probed the different regions within the cloud. Indeed, one can see in top right panel of Fig. 1 that high rotational levels of H_2 are strongly excited in the outer regions of the clouds, at low H_2 column densities, since UV pumping lines are not saturated and hence the photoexcitation rate is relatively high. Such "outer regions" of the cloud actually attributed to the diffuse atomic medium, with relatively low H_2 molecular fraction. It is likely that hydrodynamical motions and turbulence mixing can increase the size of this region. Indeed, in the static model, the H_2 abundance in the cloud is set by the balance between the formation on dust and the photodestruction by UV field, which is accompanying process to the photoexcitation, taken place in the Werner and Lyman UV lines. In the outer part of the cloud the lines are not saturated and therefore the photodestruction rate per one H_2 molecule is much higher than the rate of H_2 formation on the dust grain. Therefore the outer envelope of the cloud has relatively low H_2 molecular fraction $\sim 10^{-5}$. This is opposite in the inner self-shielded part, where photodestruction drastically dropped, due to saturation of the lines,

and the hydrogen converts to molecular form. Once we add the hydrodynamical mixing of the layers to the static model, we will get that if a self-shielded part of the medium moves to the non-self-shielded region, the hydrogen will quickly (on timescales $t_{\text{diss}} \sim (10^{10} - 10^{11}) \times I_{\text{UV}} \text{ s}$, correspond to the unshielded photoexcitation at ISM UV field) convert from molecular to dominantly atomic form. Oppositely, if atomic medium will come to the shielded region, it will take a much more time ($t_{\text{form}} \sim 10^{15} Z^{-1} \text{ s}$) to convert the hydrogen to molecular form. This qualitatively explain, why we can expect that the diffuse atomic envelope of the cloud can be more extended than ones in static models. As we already show, the high rotational levels of H_2 are significantly excited in this region and therefore one may expect enhanced excitation of these levels in comparison to the static model results. Additionally, high rotational level of H_2 can be additionally excited in outer envelopes by a turbulent dissipation, which is expected to be also enhanced in this region (e.g., Cecchi-Pestellini et al. 2005). Moreover, there is an observational signature of a such enhancement, concerned with the well established effect of the doppler parameter increase with an increase of the H_2 rotational level number (Noterdaeme et al. 2007; Balashev et al. 2009), which is naturally explained by the enhanced doppler parameter in the outer shell of the cloud (Balashev et al. 2009). Contrary, the central shielded-part of the clouds is more stable for this mixing

and the measured column densities of lower rotational levels of H₂ mostly probe the central parts. Additionally, as we already noted, the low-*J* levels mostly reflect the thermal balance in the cloud, which also is less affected to the UV radiative transfer in H₂ lines. Therefore we argue that such levels provide more reliable measurements of the physical conditions. And in the cases where the population of high rotational levels H₂ contradict with physical conditions inferred from the joint analysis of lower H₂ rotational levels and C I fine-structure levels, we report the values of the I_{UV} and n neglecting population of high rotational levels of H₂.

3 DATA SAMPLE

We compiled samples of absorption systems with measured populations of H₂ rotational levels and C I fine-structure levels at high redshift H₂-bearing DLAs and along the lines of sight towards stars in the Milky-Way and the Magellanic Clouds galaxies.

3.1 High redshift DLAs

Currently about 50 H₂-bearing DLAs are known at high redshift (e.g. see Balashev et al. 2019). We select high-*z* DLAs, which were detected in quasar spectra obtained with the Ultraviolet and Visual Echelle Spectrograph (UVES, Dekker et al. 2000) mounted on the ESO VLT-UT 2 8.2 m telescope on Cerro Paranal, Chile and the High Resolution Echelle Spectrometer (HIRES, Vogt et al. 1994) on the Keck I telescope on Maunakea in Hawaii. These spectra have a high spectral resolution ($R \geq 50\,000$ or the width of instrument function $\leq 6\text{ km s}^{-1}$) and a high signal to noise ratio ($S/N > 10$). We do not use the data for H₂-bearing DLA systems found in spectra obtained with medium spectral resolution (e.g. observed with VLT/X-shooter with $R \sim 5000 - 9000$), while such estimates are possible (see Balashev et al. 2019). This was done, to minimize a possible systematic uncertainty concerned with the determination of a velocity structure. Indeed, complex multicomponent velocity structure in H₂ lines seen in at least half of H₂-bearing DLAs, which is very hard to unambiguously resolve with intermediate resolution spectra. The high resolution spectra provide this opportunity and even allow to reliably measure the Doppler parameters of H₂ and C I absorption lines with $\sim 2 - 5\text{ km s}^{-1}$, due to large number of lines involved in analysis.

To compile a final sample we also used two additional criteria: (i) we used only H₂-bearing DLAs where C I were detected, since a joint analysis of H₂ and C I allows to significantly improve constraints. (ii) We used only the systems with the total H₂ column density higher than $\log N(\text{H}_2) \sim 18$. This was done to be sure that we really probed self-shielded regions. Additionally, we found using the closer look in PDR MEUDON results, that for most systems satisfied these criteria, low rotational levels are thermalized, i.e. T_{01} close to the kinetic temperature in the medium.

After applying these criteria, we are left with twelve H₂-bearing DLAs at $z > 1.9$, containing totally of fourteen velocity components. This sample, that we call S^{DLA} , is presented in Table 2.

3.2 Milky-Way and the Magellanic Clouds

Absorption line measurements of H₂ and C I in the ISM of galaxies in the local Universe (the Milky Way and the Small and Large Magellanic Clouds) were performed with the Far Ultraviolet Spectroscopic Explorer (FUSE) and the Space Telescope Imaging Spectrograph (STIS) on board the Hubble Space Telescope (HST). The FUSE spectra have the moderate spectral resolution (approximately $R = 20000$ or $\text{FWHM} \sim 15\text{ km s}^{-1}$) and cover the range $905 - 1180\text{ \AA}$. These spectra were used to analyse H₂ absorption systems in the Milky-Way by Snow et al. (2000); Rachford et al. (2002); Rachford et al. (2009); Jensen et al. (2010) and Magellanic Clouds by Tumlinson et al. (2002). The STIS spectra have the high spectral resolution up to $R = 114000$ or $\text{FWHM} = 2.7\text{ km s}^{-1}$ and cover the range $\lambda = 1160 - 3100\text{ \AA}$ in the E140H and E230H modes. The spectra obtained by STIS were used to analyse C I absorptions in MW by Jenkins & Tripp (2011), and LMC and SMC by Welty et al. (2016).

We selected ten and four H₂ absorption systems observed in the Milky-Way and Magellanic Clouds, respectively, in which populations of both H₂ rotational levels and C I fine-structure levels were measured. These samples, that we call S^{MW} and S^{MC} , are presented in Table 3. Each absorption system in the S^{MC} sample has several velocity components. These components are resolved in C I lines in STIS spectra, but not resolved in H₂ lines since FUSE spectra have lower spectral resolution and H₂ lines from $J < 3$ levels are highly saturated ($\log N(\text{H}_2) \sim 19 - 20$ for $J=0,1$). We assume that individual C I components are embedded in one huge cloud H₂, excitation of which is described by some average kinetic temperature. The variation in the kinetic temperature between the components is probably offset by a systematic uncertainty (± 0.3 dex), which we added to the observed population of H₂ levels. Therefore we analysed individually each C I component, but used the total rotational populations of H₂ levels.

4 RESULTS

In this section we present the constraints on the T_{kin} , I_{UV} and n_{H} obtained by an analysis of H₂ and C I excitation in high-redshift DLAs and local galaxies (Milky-Way, LMC and SMC) and discuss the obtained results. Our estimates are presented in Table 2 for the S^{DLA} sample, and in Table 3 for the S^{MW} and S^{MC} samples. The figures contain fit to H₂ and C I population, and 2D probability density functions for $I_{UV} - n$, for each systems in considered samples are presented in Appendix A.

4.1 Kinetic temperature

We used T_{01} excitation temperature as a measurement of the kinetic temperature. The T_{01} excitation temperature as a function of $\log N(\text{H}_2)$ is shown in Fig. 4. We found that T_{01} in the S^{DLA} sample is in the range of $47 - 190\text{ K}$ with the mean about $\sim 100\text{ K}$. In the S^{MW} we found slightly lower temperatures in range ($44 - 100\text{ K}$). This is not surprisingly, since S^{MW} sample probes higher H₂ column densities, due to only such systems have been studied in the HST/STIS C I survey. For these column densities, well-established trend

Table 2. The list of H_2 absorption systems included in S^{DLA} sample. The columns are: (1) name of QSO, (2) the redshifts of DLA, (3) $H\text{I}$ column densities, (4) total H_2 column density (5) total $C\text{I}$ column density, (6) an average metallicity, (7) T_{01} excitation temperature of H_2 (7), our estimates of the hydrogen number density (8) and intensity of incident UV radiation (9).

Name	z_{abs}	$\log N_{\text{HI}}^{\text{DLA}}$ [cm^{-2}]	$\log N_{\text{H}_2}$ [cm^{-2}]	$\log N_{\text{CI}}$ [cm^{-2}]	[X/H]	T_{01} [K]	$\log n_{\text{H}}$ [cm^{-3}]	$\log I_{\text{UV}}$ [Mathis unit]	Ref
J 0000+0048	2.525458	20.80±0.10	20.44±0.03	16.21±0.07	0.46±0.45	52±2	1.31 ^{+0.24} _{-0.42}	-0.19 ^{+0.28} _{-0.24}	1
B 0528-2505	2.810995	21.35±0.07	18.10±0.01	12.15 ^{+0.07} _{-0.05}	-0.91±0.07	141 ⁺⁶ ₋₆	2.22 ^{+0.21} _{-0.22}	0.90 ^{+0.14} _{-0.15}	2
J 0812+3208	2.626443	21.35±0.10	19.93±0.05	13.52±0.15	-0.81±0.10	48±2	2.26 ^{+0.21} _{-0.23}	-0.14 ^{+0.17} _{-0.17}	3
	2.626276		18.82±0.37	12.85±0.02	-0.81±0.10	50 ⁺⁴⁴ ₋₁₆	0.86 ^{+0.24} _{-0.42}	-0.95 ^{+0.34} _{-0.05}	3
J 0816+1446	3.28742	22.00±0.10	18.62 ^{+0.21} _{-0.17}	13.67±0.02	-1.10±0.10	110 ⁺³³ ₋₄₃	1.63 ^{+0.08} _{-0.12}	-0.32 ^{+0.20} _{-0.16}	4
J 0843+0221	2.786459	21.82±0.11	21.21±0.02	13.52±0.05	-1.52±0.10	123 ⁺⁹ ₋₈	1.85 ^{+0.07} _{-0.09}	1.80 ^{+0.15} _{-0.14}	5
	2.786582		21.21±0.02	13.79±0.05	-1.52±0.10	123 ⁺⁹ ₋₈	1.94 ^{+0.08} _{-0.07}	1.80 ^{+0.12} _{-0.09}	5
J 1232+0815	2.3377	20.90±0.08	19.57±0.10	14.07±0.05	-1.35±0.12	66 ⁺¹⁹ ₋₁₂	1.58 ^{+0.14} _{-0.11}	-0.55 ^{+0.21} _{-0.20}	6
J 1237+0647	2.68955	20.00±0.15	19.20 ^{+0.13} _{-0.12}	13.08±0.02	0.34±0.12	108 ⁺⁹² ₋₃₄	1.27 ^{+0.14} _{-0.10}	0.99 ^{+0.11} _{-0.15}	7
J 1439+1118	2.41837	20.10±0.10	19.52±0.07	14.64±0.03	0.16±0.11	107 ⁺³³ ₋₂₀	0.90 ^{+0.15} _{-0.18}	0.63 ^{+0.19} _{-0.17}	8
B 1444+0126	2.08696	20.25±0.07	18.15±0.10	13.18±0.10	-0.80±0.09	193 ⁺²⁸² ₋₇₀	1.94 ^{+0.26} _{-0.21}	0.49 ^{+0.16} _{-0.19}	9
J 1513+0352	2.463622	21.82±0.02	21.31±0.01	15.02±0.05	-1.22±0.10	82 ⁺⁴ ₋₄	1.90 ^{+0.13} _{-0.12}	0.45 ^{+0.24} _{-0.20}	10
J 2100-0641	3.09145	21.05±0.15	18.76±0.03	12.77±0.03	-0.73±0.15	159 ⁺⁴⁴ ₋₂₉	1.40 ^{+0.28} _{-0.35}	-0.50 ^{+0.22} _{-0.34}	11
J 2140-0321	2.3399	22.40±0.10	20.13±0.07	13.57±0.03	-1.05±0.12	75 ⁺¹² ₋₉	2.42 ^{+0.11} _{-0.09}	1.64 ^{+0.13} _{-0.21}	12

References: (1) Noterdaeme et al. (2017); (2) Klimentko et al. (2015); (3) Balashev et al. (2010); (4) Guimarães et al. (2012); (5) Balashev et al. (2017); (6) Balashev et al. (2011); (7) Noterdaeme et al. (2010); (8) Srikanand et al. (2008); (9) Ledoux et al. (2003); (10) Ranjan et al. (2018); (11) Balashev et al. (2015); (12) Noterdaeme et al. (2015).

Table 3. List of H_2 absorption systems included in S^{MW} and S^{MC} samples. The columns are the same as in Table 2, except the redshift column that is not provided, since these measurements are from local galaxies.

Name	$\log N_{\text{HI}}$ [cm^{-2}]	$\log N_{\text{H}_2}$ [cm^{-2}]	$\log N_{\text{CI}}$ [cm^{-2}]	[X/H]	T_{01} [K]	$\log n_{\text{H}}$ [cm^{-3}]	$\log I_{\text{UV}}$ [Mathis unit]	Ref
Milky-Way								
HD 24534	20.73±0.06	20.92±0.03	13.97±0.05	-0.2	57 ⁺³ ₋₃	2.62 ^{+0.10} _{-0.06}	-0.05 ^{+0.11} _{-0.11}	1,2
HD 27778	20.98±0.30	20.79±0.03	15.08±0.05	-0.2	56 ⁺⁵ ₋₅	2.04 ^{+0.13} _{-0.09}	-0.23 ^{+0.20} _{-0.17}	1,2
HD 40893	..	20.58±0.03	14.95±0.05	-0.2	78 ⁺⁹ ₋₈	1.76 ^{+0.09} _{-0.08}	-0.59 ^{+0.22} _{-0.16}	
HD 147888	..	20.48±0.03	14.23±0.05	-0.2	45 ⁺³ ₋₃	2.71 ^{+0.07} _{-0.09}	0.09 ^{+0.17} _{-0.13}	1,2
HD 185418	21.11±0.15	20.77±0.03	14.82±0.05	-0.2	101 ⁺¹⁰ ₋₈	1.81 ^{+0.06} _{-0.08}	-0.32 ^{+0.25} _{-0.17}	1,2
HD 192639	21.32±0.12	20.69±0.03	14.99±0.05	-0.2	98 ⁺⁹ ₋₉	1.94 ^{+0.08} _{-0.04}	-0.14 ^{+0.22} _{-0.21}	1,2
HD 195965	..	20.37±0.03	14.67±0.05	-0.2	110 ⁺⁷ ₋₇	1.85 ^{+0.12} _{-0.09}	-0.32 ^{+0.22} _{-0.22}	
HD 206267	21.30±0.15	20.86±0.03	15.54±0.05	-0.2	64 ⁺³ ₋₃	2.13 ^{+0.06} _{-0.08}	-0.32 ^{+0.17} _{-0.13}	1,2
HD 207198	21.34±0.17	20.83±0.03	15.53±0.05	-0.2	66 ⁺³ ₋₃	2.04 ^{+0.05} _{-0.76}	-0.28 ^{+0.18} _{-0.23}	1,2
HD 210839	21.15±0.10	20.84±0.03	14.41±0.05	-0.2	72 ⁺⁴ ₋₄	3.30 ^{+0.15} _{-0.10}	0.54 ^{+0.12} _{-0.11}	1,2
		20.84±0.03	14.99±0.05	-0.2	72 ⁺⁴ ₋₄	2.04 ^{+0.09} _{-0.05}	-0.32 ^{+0.20} _{-0.13}	
LMC								
SK -67°05	20.88 ^{+0.12} _{-0.15}	19.46±0.05	13.62±0.02	-0.4	57 ⁺⁵ ₋₄	2.22 ^{+0.13} _{-0.10}	-0.68 ^{+0.16} _{-0.20}	3,4
		19.46±0.05	13.15±0.04	-0.4	57 ⁺⁵ ₋₄	2.13 ^{+0.19} _{-0.19}	-0.86 ^{+0.20} _{-0.14}	
SK -70°115	21.37 ^{+0.12} _{-0.15}	19.94±0.07	13.25±0.04	-0.4	53 ⁺⁶ ₋₅	1.63 ^{+0.18} _{-0.17}	-0.37 ^{+0.35} _{-0.31}	3,4
		19.94±0.07	13.35±0.04	-0.4	53 ⁺⁶ ₋₅	1.81 ^{+0.12} _{-0.13}	-0.28 ^{+0.29} _{-0.27}	
		19.94±0.07	13.70±0.03	-0.4	53 ⁺⁶ ₋₅	2.31 ^{+0.16} _{-0.15}	0.04 ^{+0.26} _{-0.20}	
SMC								
SK 13	21.15±0.10	20.36±0.07	13.12±0.04	-0.7	66 ⁺⁵ ₋₅	2.08 ^{+0.14} _{-0.17}	-0.23 ^{+0.26} _{-0.20}	4,5,6
		20.36±0.07	13.51±0.09	-0.7	66 ⁺⁵ ₋₅	2.67 ^{+0.30} _{-0.24}	0.18 ^{+0.24} _{-0.23}	
		20.36±0.07	13.54±0.05	-0.7	66 ⁺⁵ ₋₅	3.12 ^{+0.25} _{-0.49}	0.18 ^{+0.10} _{-1.18}	
		20.36±0.07	13.31±0.06	-0.7	66 ⁺⁵ ₋₅	2.94 ^{+0.31} _{-0.26}	0.31 ^{+0.24} _{-0.21}	
SK 18	21.90±0.15	20.63±0.05	13.13±0.06	-0.7	53 ⁺⁴ ₋₄	1.94 ^{+0.16} _{-0.16}	-0.23 ^{+0.25} _{-0.36}	3,4,5
		20.63±0.05	14.04±0.03	-0.7	53 ⁺⁴ ₋₄	2.76 ^{+0.13} _{-0.10}	0.27 ^{+0.16} _{-0.27}	

References: (1) Jensen et al. (2010); (2) Jenkins & Tripp (2011); (3) Tumlinson et al. (2002); (4) Welty et al. (2016); (5) Rachford et al. (2002); (6) Cartledge et al. (2005)

Values of the metallicity are taken from Martín-Hernández et al. (2002) for the Milky-Way and references in Welty et al. (2016) for the LMC and SMC.

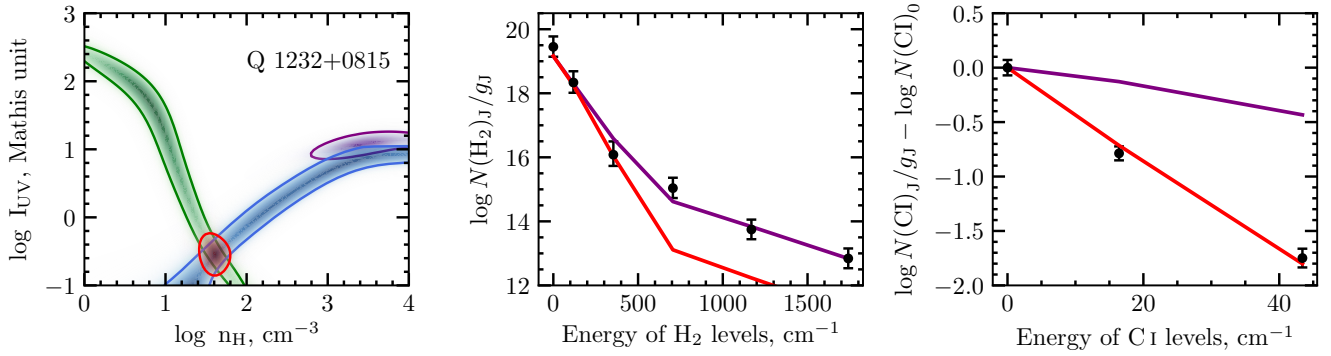


Figure 3. An example of the analysis of excitation of H_2 rotational and C I fine structure levels in the H_2 absorption system at $z = 2.3377$ towards QSO J1232+0815. In the left panel green, blue and purple contours represent the constraints on the number density and UV intensity obtained with the analysis of fine structure levels of C I, lower rotational levels of H_2 ($J=0$ to $J=2$) and both lower and higher rotational levels of H_2 ($J=0$ to $J=5$), respectively. The red contour indicate a joint constraint using C I and lower levels of H_2 . The middle and right panels show the population of H_2 rotational and C I fine structure levels, respectively. The black circles indicate the observed values. The purple lines show the model with the best fit values of the number density and UV intensity obtained from the fit to all rotational levels of H_2 ($J=0$ to $J=5$), while the red lines correspond to the joint fit to population of lower ($J=0$ to $J=2$) levels of H_2 and C I levels.

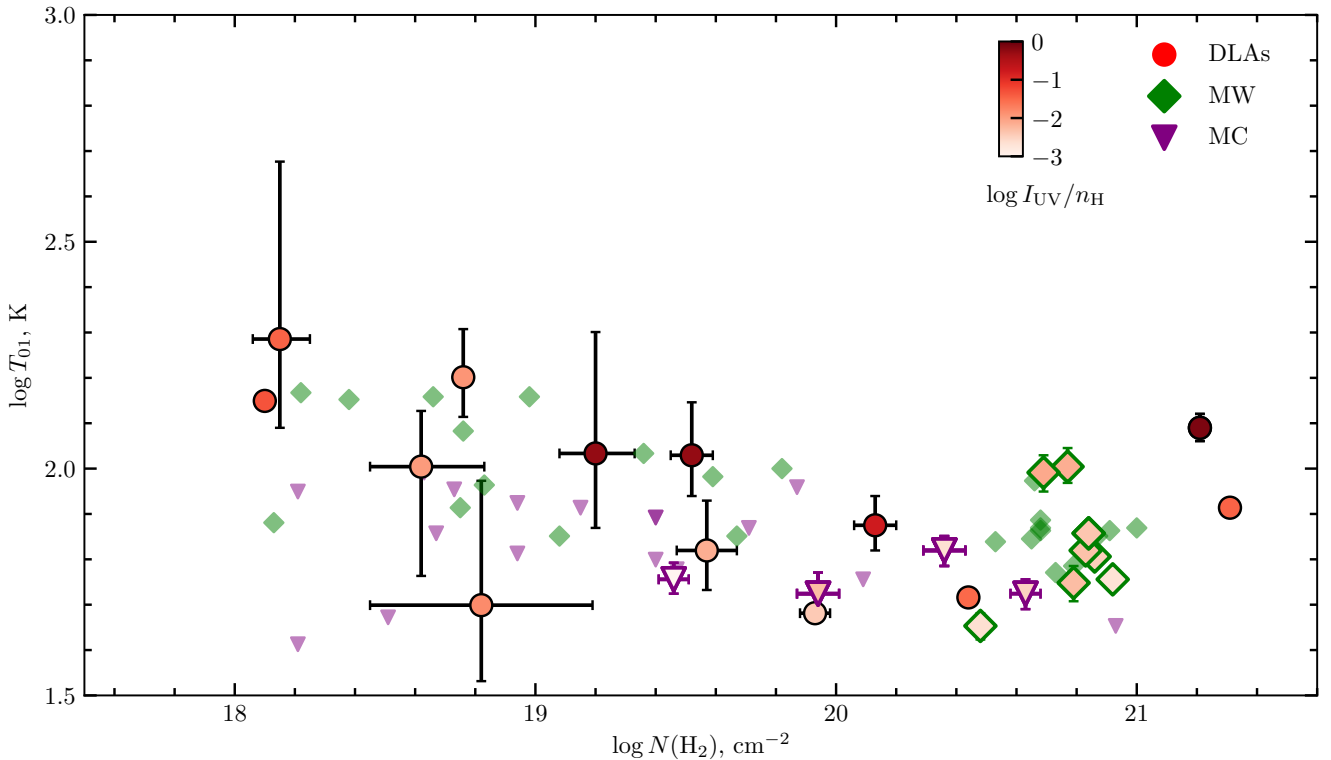


Figure 4. The excitation temperatures $T_{01}(\text{H}_2)$ as a function of the column density of H_2 systems measured in high redshift DLAs (circles), Milky-Way (diamonds) and Magellanic Clouds (triangles). Color gradient of points encodes our estimate of the ratio of the intensity of incident UV field to number density. Little green diamonds and purple triangles respectively represent known data of T_{01} in H_2 systems in the Milky-Way (Gillmon et al. 2006), SMC and LMC (Tumlinson et al. 2002).

(which was reported for both local and high- z measurements Muzahid et al. (2015); Balashev et al. (2017)) of a decrease in the T_{01} temperatures with an increase in the H_2 column density, suggests typically lower temperatures in S^{MW} . To illustrate this trend we additionally plot by little green diamonds the measurements of T_{01} in H_2 systems in the Milky-Way, where C I absorptions were not detected (Gillmon et al. 2006; Jensen et al. 2010). Based on the detailed look of the PDR models we found that this trend can be explained by an enhanced H_2 molecular fraction inside the cloud with an increase of the H_2 column density. The enhanced H_2 molecular fraction increases the cooling rate by H_2 (e.g. Le Petit et al. 2006). For $\log N(H_2) \gtrsim 19$ cooling by H_2 begins to play a significant role in the thermal balance in comparison with cooling by C II and O I lines which dominate in the atomic medium.

In the S^{MC} sample we get T_{01} within the range of 52 – 64 K, which is systematically lower than ones in the S^{DLA} and S^{MW} samples at the similar column densities (taking into account aforementioned trend). This difference is much probably attributed to the difference in the physical conditions. Indeed, we show this with a red color gradient of symbols in Fig. 4. The color encodes the ratio of UV radiation intensity to number density ($I_{\text{UV}}/n_{\text{H}}$). One can note that at specified H_2 column density the kinetic temperature increases with an increase of this ratio. This is better seen if we plot the ratio of $I_{\text{UV}}/n_{\text{H}}$ as a function of T_{01} , see Fig. 5. In the left panel we plot this relation for the S^{DLA} sample. One can see (the right panel of Fig. 5) that for a subsample, S_{19}^{DLA} , of H_2 absorption systems with $\log N(H_2) > 19$ there is an evident power law dependence over the range of $1.5 \lesssim \log T \lesssim 2.2$ with the index $\alpha_{\text{DLA}} = 5.2 \pm 0.8$. For MW sample the power law dependence is less evident, while the data formally suggests index $\alpha_{\text{MW}} = 1.3 \pm 0.2$.

Such power law dependence is naturally expected from the thermal balance that is implemented in the PDR MEUDON code. Indeed, derived estimates on I_{UV} and n_{H} are based on the observed H_2 ortho-para ratio which for saturated H_2 systems, considered here matches with kinetic temperature. The thermal balance suggests, that in diffuse ISM the cooling is dominated by C II emission and heating is mostly determined by the photoelectric heating. Roughly one can write (see e.g. eqs. (19) and (20) from Wolfire et al. 2003)

$$\frac{I_{\text{UV}}}{n_{\text{H}}} \propto T^\alpha, \quad (1)$$

where α is the index, which actually depends on the dust properties, and physical parameters, e.g. the standard combination of $I_{\text{UV}}T^{1/2}/n_e$, where n_e is the electron density (see Wolfire et al. 2003). Since metallicities (and hence electron fractions) are different in the DLA and MW samples, this can explain the difference seen in the power law indexes. Also note that MW sample is located in very tight range of $I_{\text{UV}}/n_{\text{H}}$, while DLA sample spans over three orders of magnitudes.

4.2 Number density

Derived hydrogen number densities in S^{DLA} sample are in the range 10 – 300 cm^{-3} with the average about 50 cm^{-3} . This is about ~ 5 times lower than average values of $\sim 200 \text{ cm}^{-3}$ derived in both S^{MW} and S^{MC} samples. The

most evident explanation of this difference is, that these samples probe different column densities ranges. Indeed, the MW sample corresponds to the higher end of the H_2 column density distribution, i.e. probes deeper into the cloud, where higher number densities are naturally expected. Additionally, the DLA sample probes the remote galaxies, that are predominantly "blindly" selected, i.e. selected by a cross-section. Such a technique evidently probes preferentially H_2 -bearing gas, located in outskirts of the remote galaxies. Therefore, it is reasonable to expect that absorption systems in the DLA sample corresponds to less dense gas than the gas in the MW sample, which is observed in $\sim \text{kpc}$ vicinity around the Sun.

4.3 Thermal pressure

In Fig. 6 we compare the thermal pressures ($P/k = n_{\text{H}}T_{\text{kin}}$) measured in our samples. The pressure in the S^{DLA} sample is in the range $10^{2.5} - 10^{4.4} \text{ K cm}^{-3}$ with the average about $\log P/k \sim 3.6$. Similar range of the pressure in study of high-redshift DLAs was found by Neeleman et al. (2015) using excitation of C II and Si II levels ($\log P/k = 1.5 - 5.5$ with mean 3.4 for 17 DLAs), by Jorgenson et al. (2010) using C I fine structure populations and the C I/C II ionization balance ($\log P/k = 3.9 \pm 3.7$ for 11 components in 6 DLAs) and recently by Balashev et al. (2019) applying the similar method for sample of 7 H_2 -bearing DLAs, observed with the VLT/Xshooter ($\log P/k = 4.0 \pm 0.5$). The pressure in the S^{MW} and the S^{MC} samples are in the ranges $10^{3.8} - 10^{5.2} \text{ K cm}^{-3}$ and $10^{3.3} - 10^{4.9} \text{ K cm}^{-3}$, and average values are respectively $\log P/k \sim 4.1 \pm 0.4$ and $\log P/k = 4.1 \pm 0.5$. Our estimates are higher than ones found in the survey of C I systems in the Milky-Way ($\log P/k = 3.58 \pm 0.18$) by Jenkins & Tripp (2011) and agree with the estimate of the pressure in the LMC and SMC ($\log P/k = 3.56 - 5.11$) by Welty et al. (2016).

Similar to findings in the Section 4.1, we obtained that for a subsample, S_{19}^{DLA} , of H_2 absorption systems with $\log N(H_2) > 19$ there is a strong correlation between the thermal pressure and the total hydrogen column density (see the right panel in Fig.6). Such correlation was already reported before using one-zone calculations of C I fine-structure excitation (e.g. Balashev et al. 2019). The subsample S_{19}^{DLA} suggests the following the relation: $\log p \simeq 0.5 \times (\log N(\text{H})_{\text{tot}} - 14.5)$ for $\log N(\text{H})_{\text{tot}} > 20$. We note that S_{MW} and S_{MC} samples do not indicate similar trend.

While we note that the value of H_2 column density, $\log N(H_2) > 19$, where aforementioned trends ($I_{\text{UV}}/n_{\text{H}}$ on T_{01} and P/k on $\log N(\text{H}_{\text{tot}})$) appear as our primary empirical findings, it is most likely a natural consequence of the H_1 -to- H_2 transition in the medium. Using PDR models we checked that for the systems from S^{DLA} sample with $\log N(H_2) < 19$, the gas in the cloud centers is predominantly atomic² with $f_{H_2} \equiv 2n(H_2)/n_{\text{H}} < 0.1$, while the sys-

² The position of the the H_1 -to- H_2 transition depends also on the metallicity and the ratio of $I_{\text{UV}}/n_{\text{H}}$ (Sternberg et al. 2014). However, for H_2 -bearing DLA systems from S^{DLA} sample with $\log N(H_2) < 19$ we measured similar values of the metallicity of ~ -1 and $I_{\text{UV}}/n_{\text{H}} \sim -1.7$, that gives the transition at $\log N(H_2) \sim 19$.

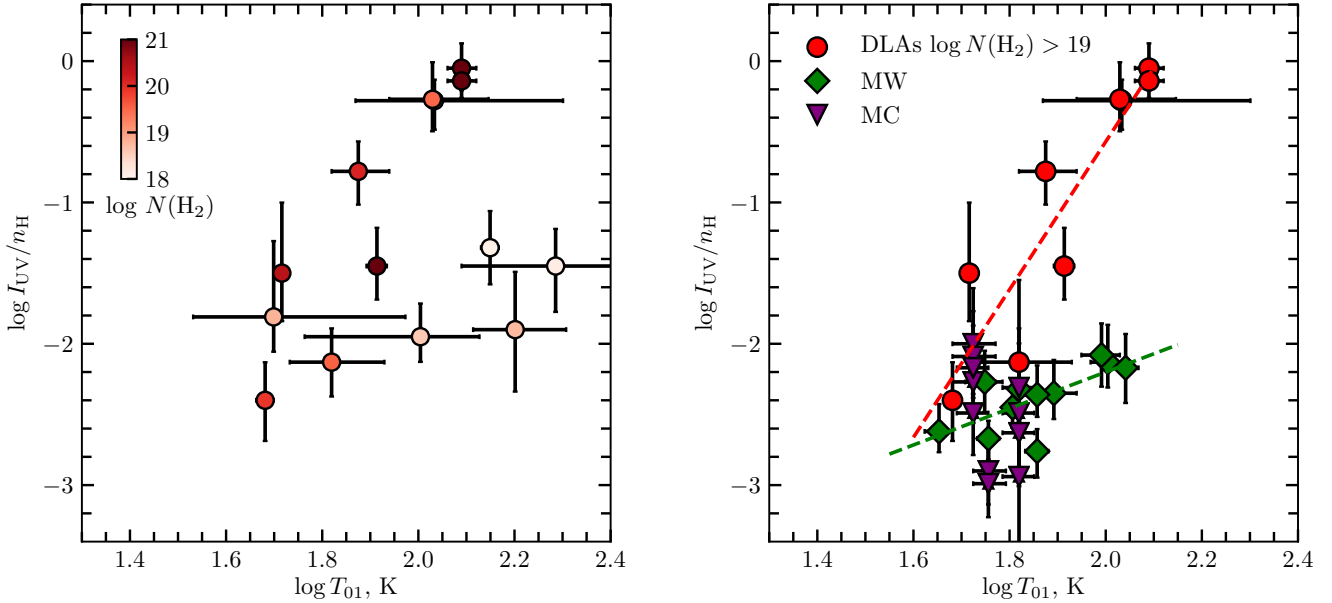


Figure 5. The ratio of the UV intensity to number density, I_{UV}/n_H , versus the excitation temperature T_{01} . The I_{UV} is in the Mathis units and n_H in cm^{-3} . In the left panel we show data for high redshift H_2 -bearing DLAs. Color gradient encodes the H_2 column density. In the right panel we compare measurements, obtained in only saturated H_2 systems with $\log N > 19$ in high redshift DLAs (red circles), Milky-Way (green diamonds) and Magellanic Clouds (purple triangles). The dashed lines represent our fit to MW and DLA samples.

tems with $\log N(\text{H}_2) > 19$ indicate high molecular fractions with $f_{\text{H}_2} \gtrsim 0.3$ (see an example of the model of J0812+3208 absorber in the top right panel in Fig. 1). That is for absorption systems $\log N(\text{H}_2) > 19$ the H I -to- H_2 transition is complete, and the thermal state of cold medium probed by these systems may be stabilized by additional cooling by H_2 lines. Hence they provide more representative constraints on the thermal pressure. The latter is increased towards the sight lines with higher hydrogen total column densities, as they probe the more central parts of the intervening galaxies (Balashev et al. 2017). This also explains the absence of $P/k - N(\text{H}_{\text{tot}})$ trend in local galaxies, since both MW and MC samples are not cross-section selected samples, since they used bright stars within the galaxies as background sources. Additionally, MW sample come from the measurement mostly within a galactic plane in the vicinity of the Solar system and the both LMC and SMC samples actually consist only from the couple of sightlines.

Additionally, based on the deeper look into PDR models, we found that the value of $\log N(\text{H}_2) > 19$ insures us that ortho-para conversion of H_2 is complete and the excitation temperature T_{01} matches the kinetic temperature, that is a direct multiplier in the thermal pressure.

4.4 Intensity of UV radiation

The intensity of the incident UV radiation and number density can be well measured by our method owing to the orthogonal dependence of regions in $I_{UV} - n_H$ plane, constrained by H_2 and C I excitation. The estimates of UV intensity for the S^{DLA} and local (S^{MW} and S^{MC}) samples are given in Table 2 and Table 3, respectively. We found that the

UV intensity in the S^{DLA} sample is varied in the wide range of 0.1 – 100 units of the Mathis field. On the contrary, the systems in the S^{MW} and S^{MC} samples are characterized by low values ranges $\sim 0.1 - 3$ units of Mathis field. The results are shown in Fig. 7.

There is a clear trend that in systems with higher UV intensity we detect higher hydrogen density n_H , which naturally consequence of the thermal balance (see also Sect. 4.1). Indeed studied systems in the samples have temperatures ~ 100 K, which evidently lead to the linear dependence of I_{UV} on n_H (see Eq. 1). However, S^{DLA} sample indicates a significant dispersion around this linear trend, some systems shown systematically higher I_{UV} (see left panel in Fig. 7). There may be different explanation of the high observed dispersion of UV intensities. However, the most straightforward one is that the S^{DLA} sample corresponds to the galaxies at redshift $z \sim 2 - 3$, where interstellar UV field is expected to be higher, since star-formation rate is peaked at these redshifts (see, e.g. Madau & Dickinson 2014). However, one should bear in mind that as a whole DLA systems (due to their selection by cross-section) probed mostly low-mass galaxies (i.e. probably not starbursts ones), that are dominated by number in galaxy population at particular redshift. Additionally the S^{DLA} sample is not typical DLAs, since only a small fraction of DLAs ($4 \pm 1\%$, see Balashev & Noterdaeme 2018) shows H_2 and hence C I absorptions (Noterdaeme et al. 2018) Therefore our measurement can indicate that UV field is statistically enhanced in the cold phase of ISM of high- z galaxies.

On the other hand one can note that S^{DLA} sample probes wide ranges of the metallicities. Actually, observed high dispersion in S^{DLA} around expected linear dependence

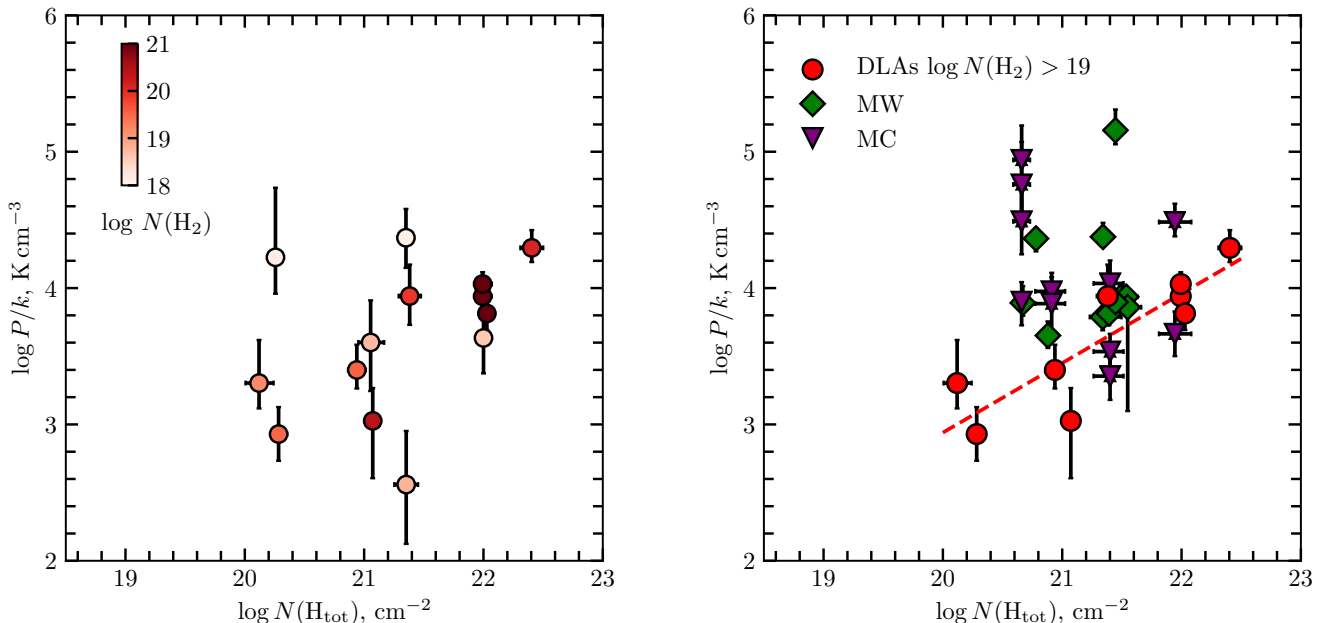


Figure 6. The dependence of the thermal pressure $P/k = n_{\text{H}}T$ on total hydrogen column density $\log N(\text{H}_{\text{tot}})$. Left panel presents the measurements in high- z H_2 -bearing DLAs. Color gradient encodes H_2 column density. The red, green and purple symbols in the right panel correspond to the measurements in saturated H_2 systems with ($\log N > 19$) for DLAs and local galaxies (Milky Way and Magellanic Clouds), respectively.

of I_{UV} on n_{H} can be reduced by correction for the metallicity. Indeed, since H_2 is formed on the dust grains, H_2 formation rate is scaled with metallicity, while H_2 destruction rate is linearly proportional to I_{UV} (Bialy & Sternberg 2016, see e.g.). It means that at low metallicities we should have lower UV flux to form H_2 at some characteristic number density. After correction for metallicity (e.g. considering I_{UV}/Z versus n_{H} plane, see the right panel of Fig. 7), the dispersion in the S^{DLA} sample around linear dependence of I_{UV}/Z on n_{H} is significantly reduced, except two systems ($J0843+0221$ and $J2140+0321$), which are extremely saturated DLAs (ESDLAs, with $\log N(\text{HI}) \geq 21.7$, Noterdaeme et al. 2014). These ESDLA systems are reasonably biased towards higher UV fluxes, since they most likely probe central parts of the remote galaxies (i.e. at very small impact parameters, see Ranjan et al. 2018, 2020), where UV flux, can be significantly enhanced on average, and locally due to higher density of star-forming regions. One can expect that such systems should be more similar to ISM clouds observed in disk of Milky-Way or Magellanic Clouds. However we see that they exhibit a higher UV field intensity, thus emphasizing the difference between local and high- z galaxies. Whether this is a common feature or a statistical outlier, it may become clear once more observations observations of such systems will be available.

5 CONCLUSION

We present a systematic study of physical conditions in the cold H_2 -bearing ISM of high redshift DLAs and in the Milky-Way and Magellanic Clouds galaxies. Our measurements

based on the fit to the observed populations of H_2 rotational levels and fine-structure levels of CI in known absorption systems, detected in spectra of high redshift quasars and stars in local galaxies.

The modelling of H_2 levels population requires an accurate calculation of the radiative transfer, and therefore only in several specific cases the detailed analysis of H_2 and CI excitation has been done. To analyse all known $\text{H}_2/\text{C}\text{I}$ systems we calculated grids of constant-density model, which were uniformly distributed in the space of three main physical parameters – the metallicity, hydrogen density and intensity of UV field. For modelling H_2 and CI level populations we used the PDR Meudon code (Le Petit et al. 2006), which performs a complete calculation of the radiative transfer of UV radiation in the UV lines of H_2 in combination with a solution of the thermal balance and chemistry. We found that in many cases a joint analysis of low H_2 rotational levels and CI fine-structure levels allows one to break the degeneracy in the $I_{\text{UV}} - n_{\text{H}}$ plane and provides significantly tighter constraints on the number density and intensity of UV field.

We applied this method to analyse physical conditions in the samples of twelve strong H_2 -bearing high redshift DLAs and fourteen CI -bearing H_2 absorption systems in the Milky-Way and Magellanic Clouds. We found that H_2 -bearing gas in these systems is cold with typical kinetic temperature ~ 100 K and dense with the number density $10 - 500 \text{ cm}^{-3}$. The values of the temperature, number density and thermal pressure are in good agreement between these three samples. However, we found that the intensity of UV field in the sample of DLAs is varied in wide range $0.1 - 100$ units of Mathis field, while it is $\sim 0.1 - 3$ units in the samples of H_2 systems in the Milky-Way and Mag-

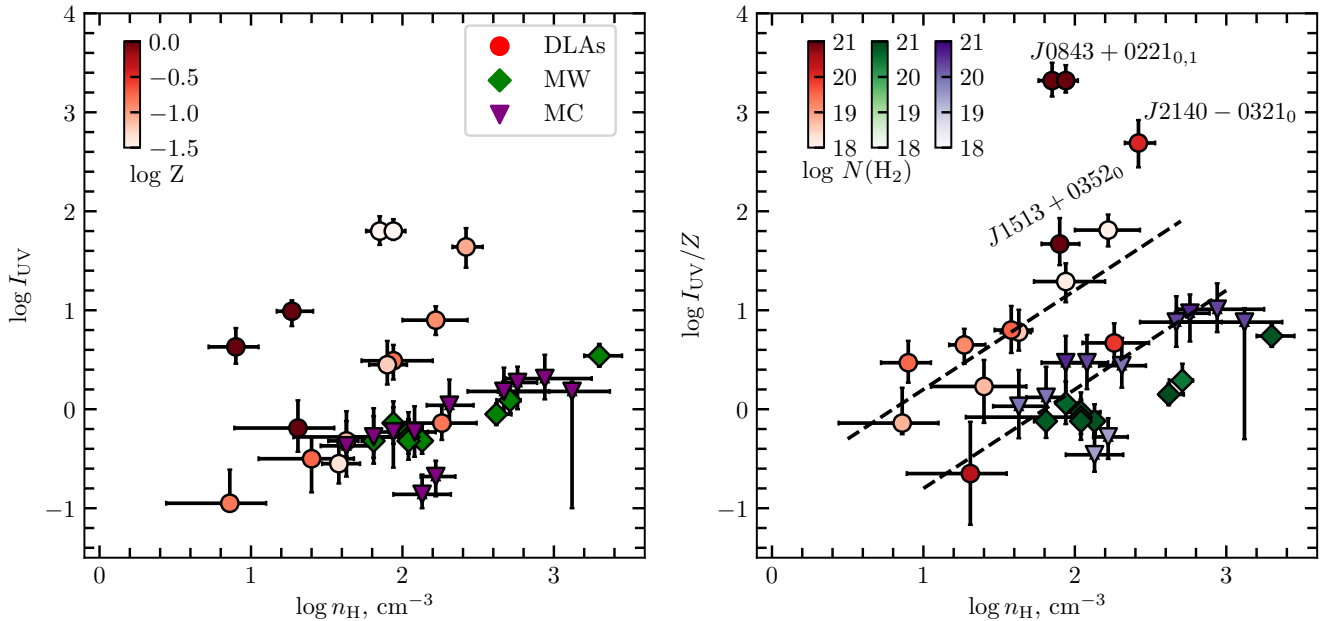


Figure 7. Left and right panels respectively show the dependence of the UV intensity and the ratio of UV intensity to metallicity on the number density. The red circles, green diamonds and purple triangles represent values derived in high redshift DLAs and H₂ systems in the Milky-Way and Magellanic Clouds, respectively. The color gradients in the left and right panels encode the metallicity and H₂ column density, respectively. The dashed lines on the right panel represent a linear dependence of the I_{UV}/Z on the hydrogen number density. Color gradient encodes the metallicity of the DLA sample in the left panel and the column density of H₂ for the samples of DLAs, Milky-Way and Magellanic Clouds in the the right panel.

ellanic Clouds. The large dispersion and measured values of UV field in DLAs sample is naturally expected, since it probes the population of the distant galaxies at redshifts $z > 2$, where the interstellar UV field can be higher, due to the peak of star-formation at these redshifts. We found that for S^{DLA} sample the dispersion around dependence of I_{UV}/Z on n_H is significantly less than dispersion around dependence of I_{UV} on n_H . This most likely linked with the scaling of H₂ formation rate with these parameters.

For a subsample of H₂ absorption systems with $\log N(\text{H}_2) > 19$ we found a linear trend of increase of UV field intensity with increasing number density and confirm the trend of increase of thermal pressure with total hydrogen column density. The first trend is naturally expected from the ISM thermal balance, while the second trend confirm the earlier findings that the higher column density DLAs probe the central parts of the remote galaxies, where the thermal pressure is enhanced. Our findings indicate that the study of the H₂/C I-bearing DLAs is very promising tool to get insights of the physical state of the cold diffuse ISM of local and high-redshift galaxies.

6 DATA AVAILABILITY

The paper is based on the published measurements of the H₂/C I-bearing absorption systems at high redshifts and local galaxies.

ACKNOWLEDGEMENTS

This work is partially supported by RFBR 18-32-00701. SB is partially supported by Basis foundation.

APPENDIX A: DETAILED FIT

In this section we present fit to observed populations of rotational levels of H₂ and fine-structure levels of C I in the S^{DLA} , S^{MW} and S^{MC} samples. In Figs A1-A7 we show constraints on the hydrogen number density n_H and UV field strange (in left panels) and best fit to population of H₂ rotational levels (middle panel) and relative populations of excited C I fine-structure levels (right panels). Systems are arranged in increasing order of coordinates.

REFERENCES

- Abgrall H., le Bourlot J., des Forêts G. P., Roueff E., Flower D. R., Heck L., 1992, *A&A*, 253, 525
- Balashev S. A., Noterdaeme P., 2018, *MNRAS*, 478, L7
- Balashev S. A., Varshalovich D. A., Ivanchik A. V., 2009, *Astron. Lett.*, 35, 14
- Balashev S. a., Ivanchik A. V., Varshalovich D. a., 2010, *Astron. Lett.*, 36, 761
- Balashev S. A., Petitjean P., Ivanchik A. V., Ledoux C., Srianand R., Noterdaeme P., Varshalovich D. A., 2011, *MNRAS*, 418, 357
- Balashev S. A., Noterdaeme P., Klimenko V. V., Petitjean P.,

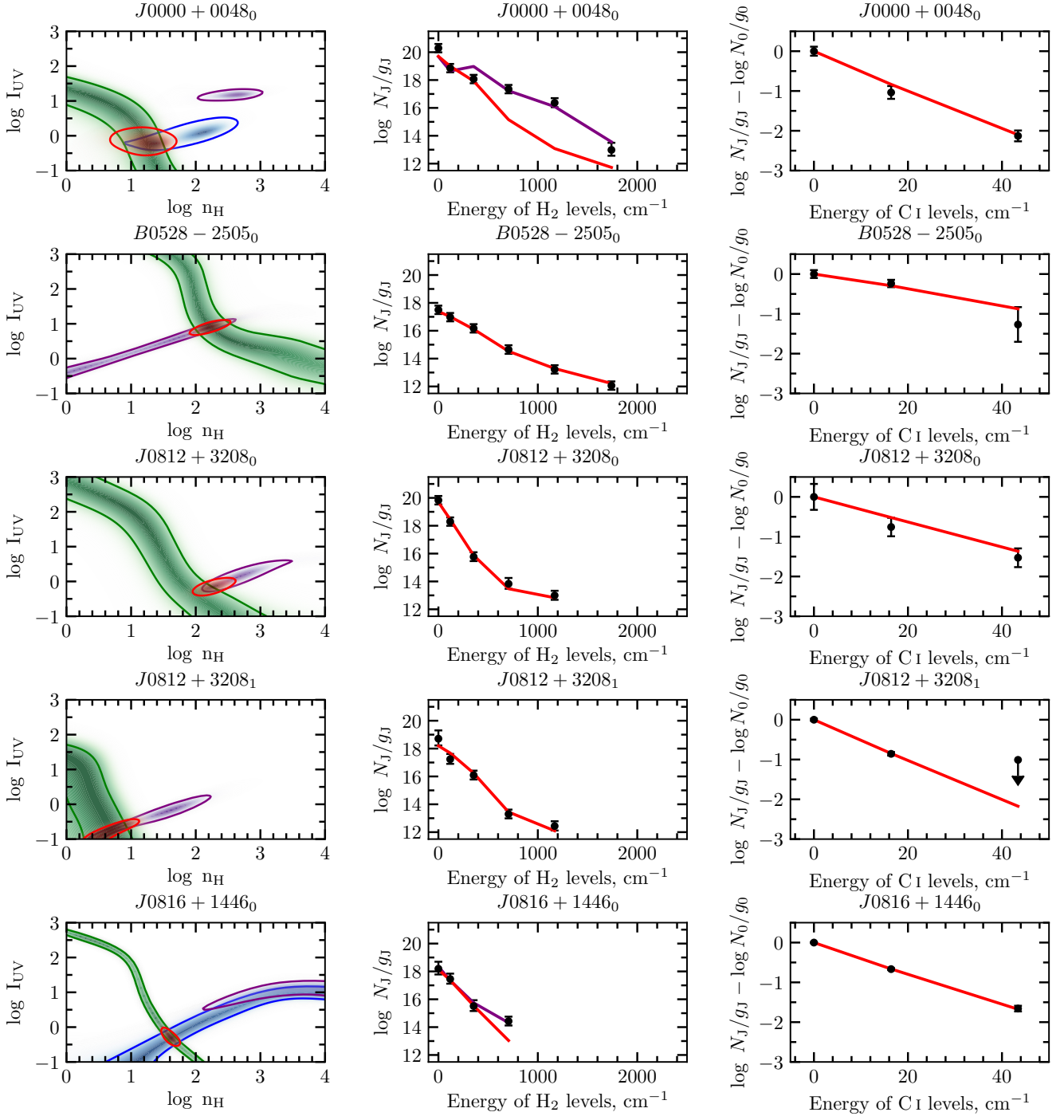


Figure A1. Fit to observed populations of H_2 and $C\text{I}$ levels in the S^{DLA} sample. In the left panel the green and purple contours represent constraints on the hydrogen number density and UV radiation intensity, obtained with the analysis of excitation of $C\text{I}$ fine-structure and H_2 rotational levels (all observed), respectively. In some cases, we also show constraint obtained with the fit to excitation of lower rotational levels of H_2 ($J=0$ to $J=2$) by the blue contour. Red contour represents a joint constraint using $C\text{I}$ and (lower) H_2 levels (if the blue contour is presented). The middle and right panels show the population of H_2 rotational and $C\text{I}$ fine-structure levels, respectively. The black circles indicate the observed values. The red lines correspond to the joint fit to population of both H_2 and $C\text{I}$ levels. The purple lines, presented in some middle panels, show the best fit obtained using only all observed H_2 rotational levels.

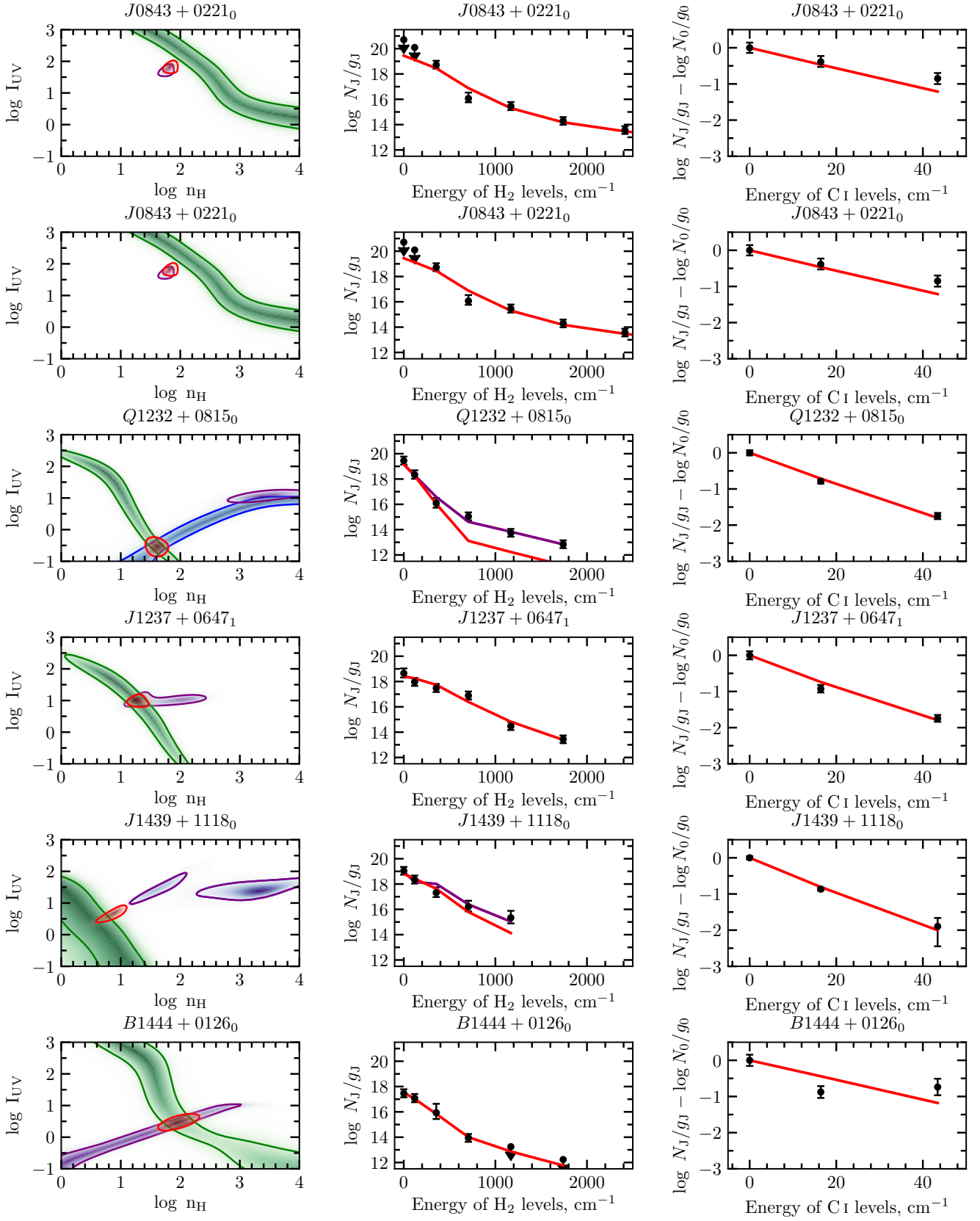


Figure A2. Continuation of Fig. A1

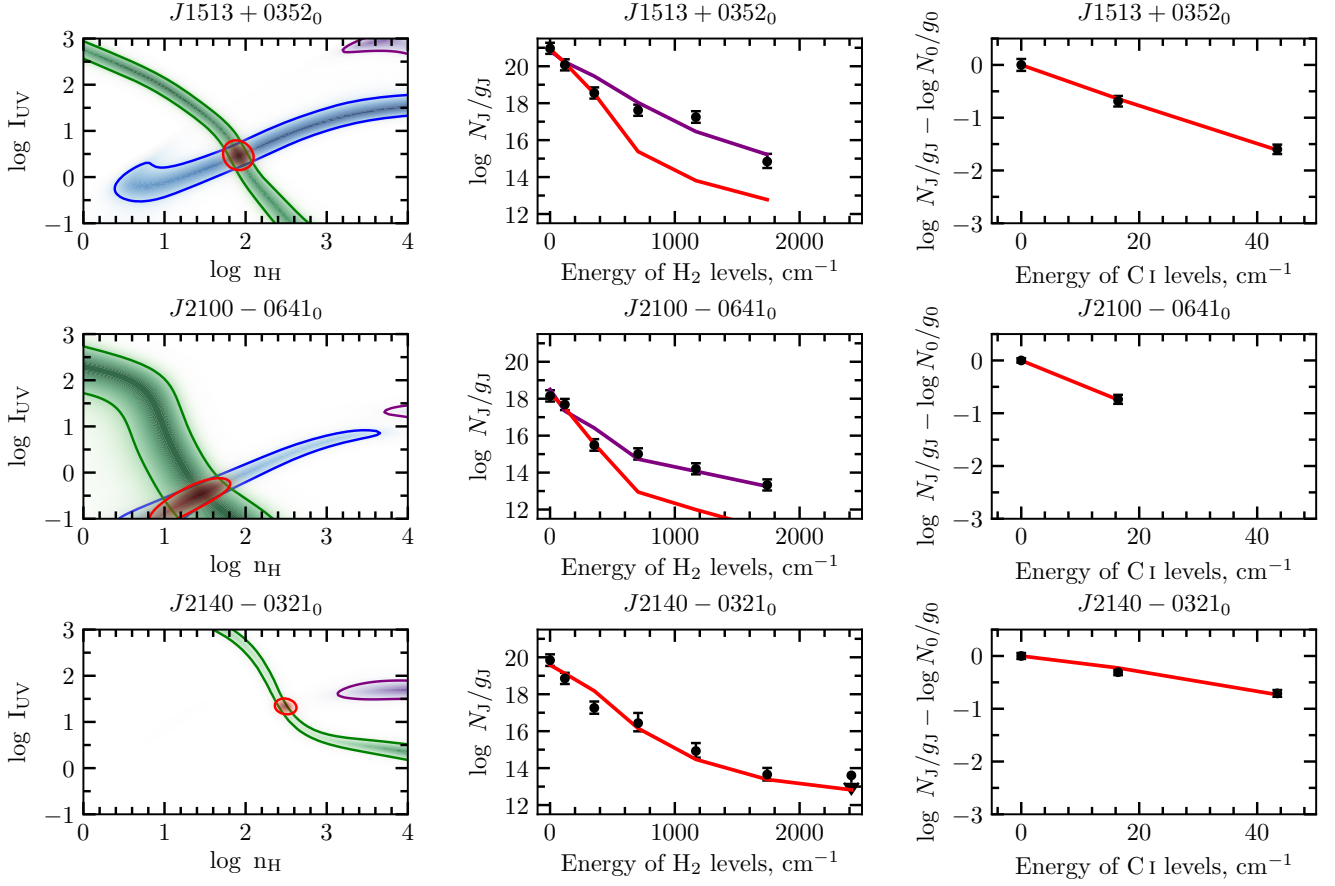


Figure A3. Continuation of Fig. A1

Srianand R., Ledoux C., Ivanchik A. V., Varshalovich D. A., 2015, *A&A*, 575, L8
 Balashev S. A., et al., 2017, *MNRAS*, 470, 2890
 Balashev S. A., et al., 2019, *MNRAS*, 490, 2668
 Bialy S., Sternberg A., 2016, *ApJ*, 822, 83
 Black J. H., Dalgarno A., 1976, *ApJ*, 203, 132
 Cartledge S. I. B., et al., 2005, *ApJ*, 630, 355
 Cecchi-Pestellini C., Casu S., Dalgarno A., 2005, *MNRAS*, 364, 1309
 Dekker H., D’Odorico S., Kaufer A., Delabre B., Kotzlowski H., 2000, *Proc. SPIE, Opt. IR Telesc. Instrum. Detect. Masanori Iye; Alan F. Moorwood; Eds.*, 4008, 534
 Draine B. T., 1978, *ApJS*, 36, 595
 Draine B. T., 2011, *Physics of the Interstellar and Intergalactic Medium*. Princeton University Press
 Gillmon K., Shull J. M., Tumlinson J., Danforth C., 2006, *ApJ*, 636, 891
 Guimarães R., Noterdaeme P., Petitjean P., Ledoux C., Srianand R., López S., Rahmani H., 2012, *AJ*, 143, 147
 Howk J. C., Wolfe A. M., Prochaska J. X., 2005, *ApJ*, 622, L81
 Indriolo N., Geballe T. R., Oka T., McCall B. J., 2007, *ApJ*, 671, 1736
 Jenkins E. B., Tripp T. M., 2011, *ApJ*, 734
 Jensen A. G., Snow T. P., Sonneborn G., Rachford B. L., 2010, *ApJ*, 711, 1236
 Jorgenson R. a., Wolfe A. M., Prochaska J. X., 2010, *ApJ*, 722, 460
 Jura M., 1975a, *ApJ*, 197, 575
 Jura M., 1975b, *ApJ*, 197, 581

Klimenko V., Balashev S., Ivanchik A., Ledoux C., Noterdaeme P., Petitjean P., Srianand R., Varshalovich D., 2015, *MNRAS*, 448
 Klimenko V., Balashev S., Ivanchik A., Varshalovich D., 2016, *Astron. Lett.*, 42
 Kulkarni V. P., Meiring J., Som D., Péroux C., York D. G., Khare P., Lauroesch J. T., 2012, *ApJ*, 749, 176
 Le Petit F., Nehmé C., Le Bourlot J., Roueff E., 2006, *ApJS*, 164, 506
 Ledoux C., Petitjean P., Srianand R., 2003, *MNRAS*, 346, 209
 Ledoux C., Noterdaeme P., Petitjean P., Srianand R., 2015, *A&A*, 580, id.A8
 Madau P., Dickinson M., 2014, *Annu. Rev. Astron. Astrophys.* vol. 52, p.415-486, 52, 415
 Martín-Hernández N. L., et al., 2002, *A&A*, 381, 606
 Mathis J. S., Mezger P. G., Panagia N., 1983, *A&A*, 500, 259
 Muzahid S., Srianand R., Charlton J., 2015, *MNRAS*, 448, 2840
 Muzahid S., Kacprzak G. G., Charlton J. C., Churchill C. W., 2016, *ApJ*, 823, id.66
 Neeleman M., Prochaska J. X., Wolfe A. M., 2015, *ApJ*, 800, id.7
 Nehmé C., Le Bourlot J., Boulanger F., Pineau Des Forêts G., Gry C., 2008, *A&A*, 483, 485
 Noterdaeme P., Ledoux C., Petitjean P., Petit F. L., Srianand R., Smette A., 2007, *A&A*, 474, 16
 Noterdaeme P., Ledoux C., Petitjean P., Srianand R., 2008, *A&A*, 481, 327
 Noterdaeme P., Petitjean P., Ledoux C., Lopez S., Srianand R., Vergani S. D., 2010, *A&A*, 523, 17
 Noterdaeme P., Petitjean P., Paris I., Cai Z., Finley H., Ge J.,

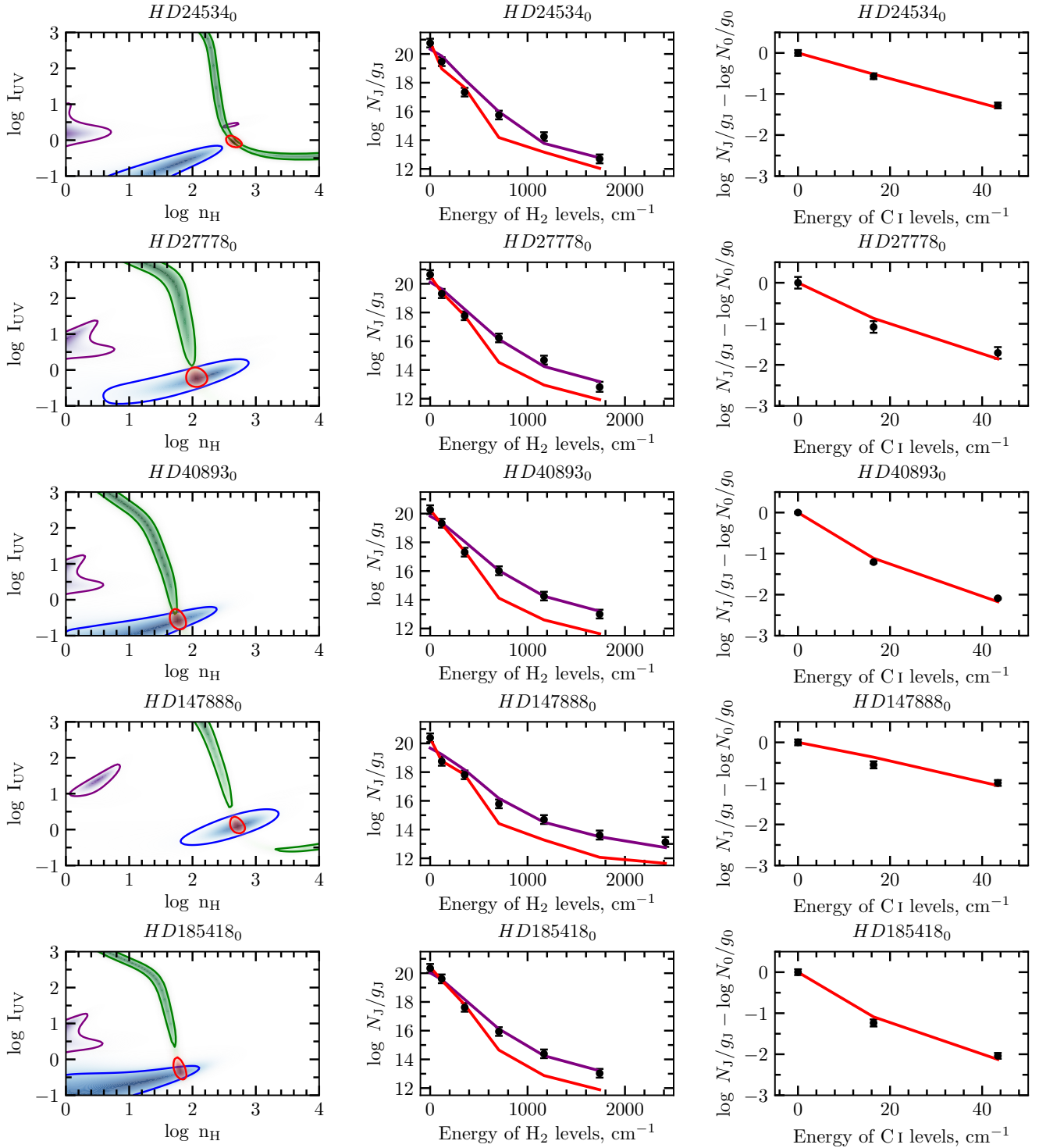


Figure A4. Fit to populations of H₂ and C I levels in the sample of H₂ absorption systems observed in the Milky-Way. The contours, lines and color encoding are the same as in Fig. A1.

Pieri M. M., York D. G., 2014, *A&A*, 566, A24
 Noterdaeme P., Srianand R., Rahmani H., Petitjean P., Pâris I.,
 Ledoux C., Gupta N., López S., 2015, *A&A*, 577, id.A24
 Noterdaeme P., et al., 2017, *A&A*, 597, 82
 Noterdaeme P., Ledoux C., Zou S., Petitjean P., Srianand R.,

Balashev S., López S., 2018, *A&A*, 612, A58
 Rachford B. L., et al., 2002, *ApJ*, 577, 64
 Rachford B. L., et al., 2009, *ApJS*, 180, 125
 Ranjan A., et al., 2018, *A&A*, 618, A184
 Ranjan A., Noterdaeme P., Krogager J. K., Petitjean P., Srianand

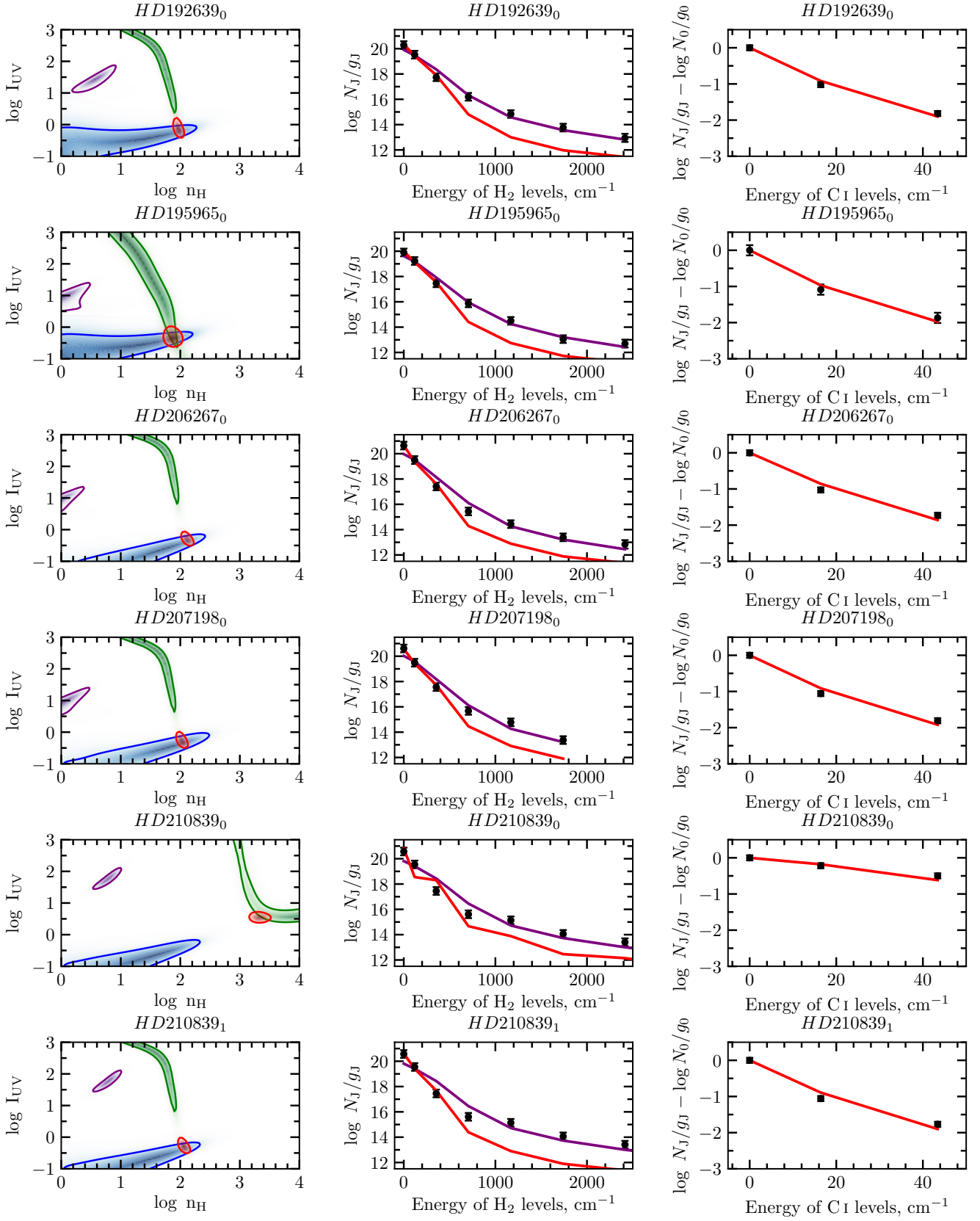


Figure A5. Continuation of Fig. A4

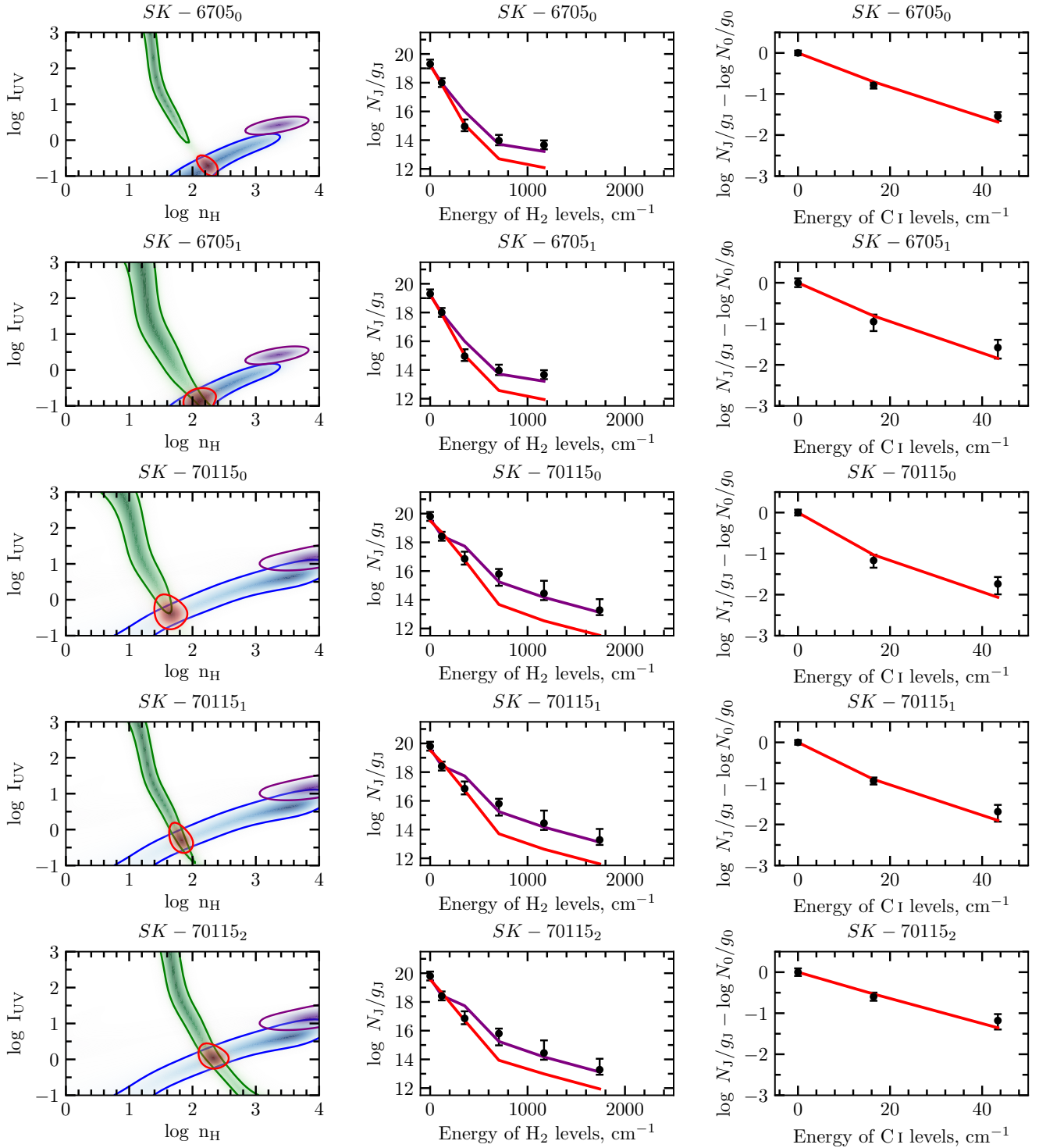


Figure A6. Fit to populations of H₂ and C I levels in the sample of H₂ absorption systems observed in the Large Magellanic Cloud. The contours, lines and color encoding are the same as in Fig. A1.

R., Balashev S. A., Gupta N., Ledoux C., 2020, *A&A*, 633, A125
 Rawlins K., Shaw G., Srianand R., 2016, *MNRAS*, 459, 3234
 Rawlins K., Srianand R., Shaw G., Rahmani H., Dutta R., Chacko S., 2018, *MNRAS*, 481, 2083

Shaw G., Ferland G. J., 2020, *MNRAS*, 493, 5153
 Silva A. I., Viegas S. M., 2002, *MNRAS*, 329, 135
 Snow T. P., et al., 2000, *ApJ*, 538, L65
 Srianand R., Petitjean P., 2000, *A&A*, p. 414
 Srianand R., Petitjean P., Ledoux C., Ferland G., Shaw G., 2005,

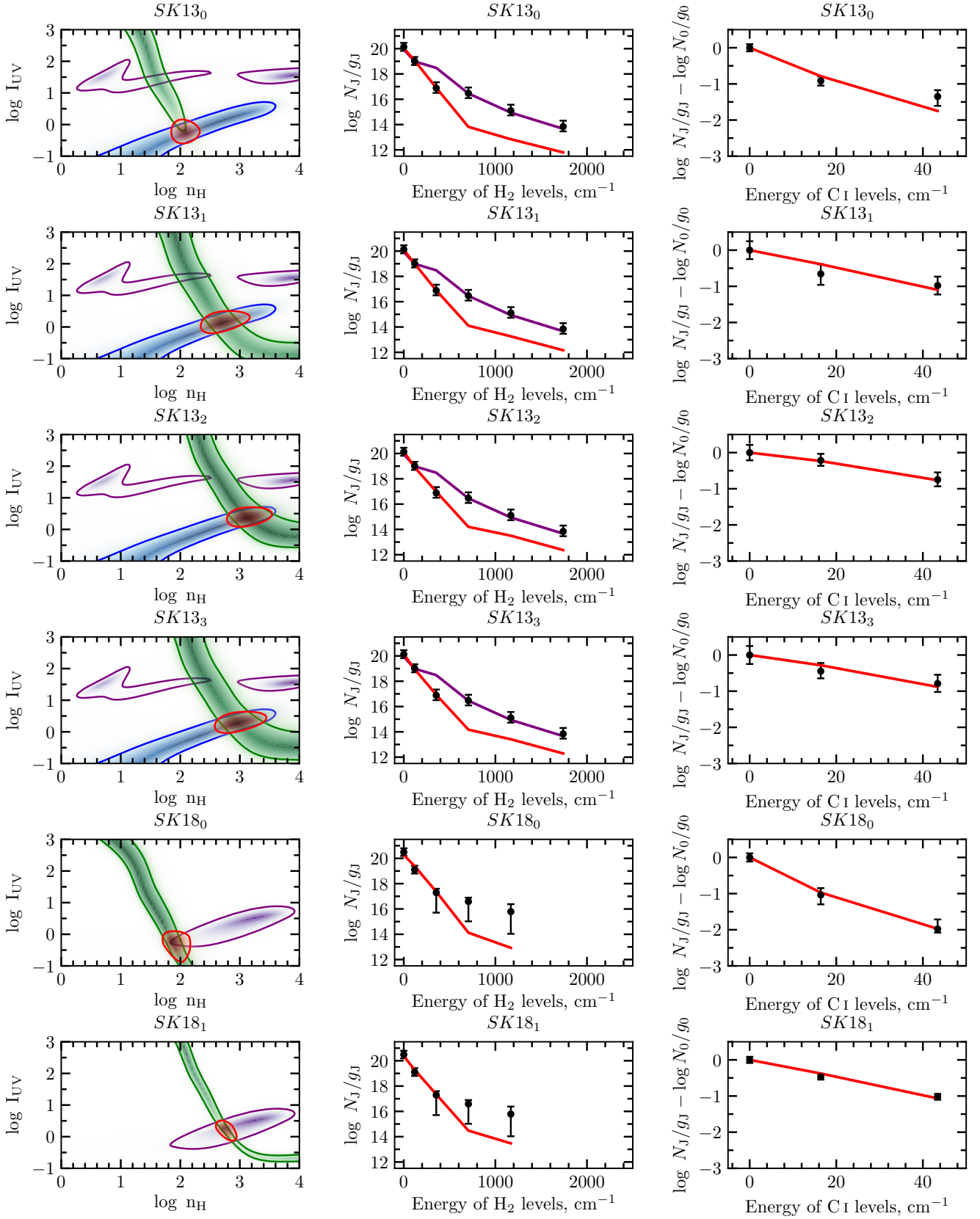


Figure A7. Fit to populations of H₂ and C I levels in the sample of H₂ absorption systems observed in the Small Magellanic Cloud. The contours, lines and color encoding are the same as in Fig. A1.

- MNRAS, 362, 549
- Srianand R., Noterdaeme P., Ledoux C., Petitjean P., 2008, *A&A*, 482, L39
- Sternberg A., Le Petit F., Roueff E., Le Bourlot J., 2014, *ApJ*, 790, 10
- Tumlinson J., et al., 2002, *ApJ*, 566, 857
- Vogt S. S., et al., 1994, in Crawford D., Craine E., eds, *Society of Photo-Optical Instrumentation Engineers (SPIE) Conference Series Vol. 2198, Proc. SPIE Vol. 2198*. pp 362–375, doi:10.1117/12.176725, [http://proceedings.spiedigitallibrary.org/proceeding.aspx?articleid=959834](http://adsabs.harvard.edu/abs/1994SPIE.2198..362Vhttp://proceedings.spiedigitallibrary.org/proceeding.aspx?articleid=959834)
- Welty D. E., Lauroesch J. T., Wong T., York D. G., 2016, *ApJ*, 821, 118
- Wolfire M. G., McKee C. F., Hollenbach D., Tielens A. G. G. M., 2003, *ApJ*, 587, 278

This paper has been typeset from a $\text{\TeX}/\text{\LaTeX}$ file prepared by the author.